Wind retrieval from temperature measurements from the Rover Environmental Monitoring Station/Mars Science Laboratory

Álvaro Soria-Salinas [a,*], María-Paz Zorzano [b,a], Roberto Mantas-Nakhai [a], Javier Martín-Torres [a,c,d]

[a] *Division of Space Technology, Department of Computer Science, Electrical and Space Engineering, Luleå University of Technology, 971 87 Luleå, Sweden*
[b] *Centro de Astrobiología (CSIC-INTA), Torrejón de Ardoz, 28850 Madrid, Spain*
[c] *Instituto Andaluz de Ciencias de la Tierra (CSIC-UGR), 18100 Granada, Spain*
[d] *School of Geosciences, University of Aberdeen, Meston Building, King's College, Aberdeen, AB24 3UE, UK*

ARTICLE INFO

ABSTRACT

This work presents a novel method for the real-time retrieval of wind speed on the surface of Mars that uses temperature measurements from the Rover Environmental Monitoring Station (REMS) instrument onboard the Curiosity rover of the Mars Science Laboratory (MSL) mission. After final failure of the Wind Sensor (WS) in sol 1491, REMS has not been providing wind data. The new wind retrieval approach that we propose may eventually be able to supply MSL with wind values for contextualizing the rover's operations and for meteorological studies on the surface of Mars. The new method is based on forced convection modeling of the Air Temperature Sensors (ATS) of REMS as thin rods immersed in the extreme low-pressure and high-radiating atmospheric conditions of the Martian thermal boundary layer at a height of ~ 1.5 m from the surface. A preliminary validation of the possibilities and limitations of this retrieval has been performed using comparative analysis with existing REMS wind field-site data for the same sols that are available at the Planetary Data System (PDS). We have developed both a "coarse" approach, in which wind speed is determined with no regard to wind direction, and a "refined" method, in which it is attempted to determine both wind speed and direction. Assuming the previously reported WS retrieval errors of 20% for the wind speed, we report an agreement to the WS values of wind speed ranging from 36.4% to 77% of the acquisition time for the "coarse" approach, depending on the sol examined. These promising results are limited to only evening extended acquisitions from 18:00 to 21:00 local mean solar time (LMST). This method could be applied to daytime conditions. The results suggest a new optimal orientation for wind speed retrieval of +60° clockwise with respect to the forward direction of the Curiosity rover, although the technique is not yet ready to be considered for planning of the Curiosity rover operations. This method could extend the wind characterization of the Gale Crater for future Curiosity rover data acquisitions by recycling air temperature measurements and provide the scientific community with a data set for future comparative analysis with the Temperature and Wind Sensors for InSight (TWINS)/InSight, the HabitAbility: Brines, Irradiation and Temperature (HABIT)/ExoMars 2022, and the Mars Environmental Dynamics Analyzer (MEDA)/Mars 2020 rover instruments.

1. Introduction

The lack of characterization of high-rate winds on the surface of Mars still represents a challenge for the scientific community that must be addressed because it has implications in a wide range of fields. The role of wind in lifting dust from the surface and its subsequent effects on atmospheric thermal radiation and boundary layer dynamics have been intensively discussed. It is believed that near-surface wind stress is responsible for lifting much of the dust from the Martian surface, particularly during dust storms (Newman et al.,

2002a; Kahre et al., 2006; Basu and Richardson, 2004). The former occurs when near-surface winds exceed a threshold speed. Therefore, knowing the near-surface wind speed is essential to understanding the dust cycle, which is in turn vital to understanding planetary boundary layer (PBL) dynamics on Mars, as well as the effects on planetary surface missions in terms of radiation; the thermal environment; entry descent and landing (EDL) stages; and dust accumulation (Madeleine et al., 2011; Hassler et al., 2014; Vicente-Retortillo et al., 2015). Furthermore, proper characterization of the PBL and near-surface wind

---

dynamics may be needed to explain the observed variability in dust and trace gases, such as methane, on Mars (Fonseca et al., 2018). However, the accurate evaluation of the performance of numerical models within the PBL at the surface requires observation of wind data, as well as other environmental parameters such as pressure and temperature (Pla-Garcia et al., 2016; Rafkin et al., 2016; Newman et al., 2017). Aeolian processes, which are driven by the near-surface wind field, are considered as the major responsible for the Martian dust cycle (Haberle et al., 1982; Newman et al., 2002a,b; Kahre et al., 2006; Cantor et al., 2006) and the likely dominant force of the evolution of the surface features of Mars (Greeley et al., 2006; Wilson and Zimbelman, 2004). In particular, transverse aeolian ridges (TARs) could be used as Martian climate-change indicators; although these features are not currently active, understanding them provides information regarding the wind-induced transport of sediments over large distances (Berman et al., 2018). Similarly, wind characterization could help in defining the planetary-protection (PP) requirements for future human exploration on Mars in terms of the natural transport of contamination, as current global circulation models (GCM) are not accurate enough for this purpose. These developments require in-situ wind measurements (Race et al., 2015; Kminek et al., 2018).

The very low-pressure and low-temperature regime on the surface of Mars, with representative values of 700 Pa and 240 K, respectively, and the amount of dust particles in suspension, especially during dust storms (Zurek, 1982), create a rapidly changing airflow around any sensor that is sent to the surface of the planet. These factors make wind retrieval particularly difficult when the device also requires extra robustness to survive the extreme environmental conditions and the severe stress that spacecraft probes have to withstand during entry, descent, and landing. Several solutions have been adopted in this scenario (Wilson, 2003), although only four surface missions, in addition to the current Mars Science Laboratory (MSL) mission, have provided useful data of the wind-surface pattern (Martínez et al., 2017a; Newman et al., 2017). With the exception of the Phoenix spacecraft, which carried the "Telltale" wind sensor based on the deflection of a Kapton tube hanging in Kevlar fibers and recorded by a camera (Holstein-Rathlou et al., 2010), thermal sensors have been the preferred approach when measuring wind speed and direction on the surface of Mars. From the NASA Viking landers 1 and 2 (Jones et al., 1979; Hess et al., 1977; Chamberlain et al., 1976), which used hot-film wind sensors, to the NASA Mars Pathfinder (Schofield et al., 1997; Sullivan et al., 2000), which included six hot wires that were evenly distributed at the top of a mast and could only provide wind direction data, thermal anemometry has been implemented as the preferred solution. This technique is mainly based on the analysis of variations in heat transfer between hot wires and the surrounding airflow. Other missions, which unfortunately failed to land successfully, used this approach, such as the thermal sensors of the Mars Polar Lander (MPL) (Polkko et al., 2000) or the Beagle 2 wind sensor (Towner et al., 2004), which used a similar concept to Pathfinder. This trend was also followed by the Rover Environmental Monitoring Station (REMS) (Domínguez et al., 2008; Gómez-Elvira et al., 2012; Gómez-Elvira et al., 2014) onboard the MSL rover Curiosity, which has been operating on Mars since 2012. Furthermore, subsequent missions to Mars also use wind sensors based on thermal anemometry. This is the case of the Temperature and Wind Sensors for InSight (TWINS)/InSight (Velasco and Rodríguez-Manfredi, 2015), whose design is based on the booms of the REMS instrument. A similar concept will be used in the Mars Environmental Dynamics Analyzer (MEDA)/NASA Mars 2020 rover (Tamppari et al., 2015).

In the case of the HabitAbility: Brines, Irradiation and Temperature (HABIT) instrument onboard the ESA-Roscosmos ExoMars 2022 mission, no dedicated wind sensor was included. Following the thermal anemometry approach that has proven reliable in past, present, and future missions to the surface of Mars, a wind retrieval algorithm has been developed to use the three Air Temperature Sensors (ATS) of the instrument as wind sensors. This approach is robust because

the hardware is even simpler than active thermal anemometry, which is based on maintaining a constant temperature difference between temperature transducers through a sigma-delta modulator (Makinwa and Huijsing, 2001, 2002; Domínguez et al., 2008). Additionally, this approach is efficient and cost-effective, with no extra power or hardware required for the retrieval. These ATS are similar to the ATS of the REMS instrument and TWINS; therefore, the successful implementation of this retrieval could yield in-situ and high-rate wind speed and direction data at different locations on Mars simultaneously. Any added measurement of surface winds is critical because a single instrument in a specific location is insufficient for characterization of the entire planet (Viúdez-Moreiras et al., 2019a).

In this work, we present a new wind retrieval method based on temperature data from the REMS ATS, which are available at the NASA Planetary Atmospheres Node of the Planetary Data System (PDS) (Gómez-Elvira, 2013a,b,c). To illustrate the concept, its potential, and its limitations, we compare it here with the REMS Wind Sensor (WS) 5-min average data from the surface of Mars. We developed this method as a potential alternative to the REMS WS, which ended operations in sol 1491, and it could provide additional value to both the HABIT/ExoMars 2022 and TWINS/InSight instruments. Previous research with a similar purpose was conducted in past missions such as the reconstruction of Viking Lander wind sensor data from its unheated cylinders, as described by Murphy et al. (1990) and Kynkäänniemi et al. (2017), which proved the usefulness of such research to maximize the output of a Martian scientific mission. The technique is still under development and cannot yet retrieve wind directions. Also, the method is currently only applicable to evening hours because direct solar radiation is not included in the model. The method depends on the location of the ATS on the operating platform, but it could be applied to other missions with a few minor modifications. Section 2 describes the operation, constraints, and limitations of the REMS WS and ATS on the surface of Mars. Section 3 focuses on the hypothesis and assumptions that we adopted for the development of the retrieval, according to the limitations of the sensor data where the retrieval is applied. Section 4 discusses the results of the validation, which was performed through a comparative analysis of the retrieval with REMS WS data on Mars for specific mission sols and an estimation of the agreement of the model with respect to the REMS data. The main conclusions are detailed in Section 5.

2. Wind and air temperature sensors

The physical concepts that define the functioning of the WS and ATS are briefly described here so that their limitations, advantages, and differences can be fully understood and to allow for a meaningful comparison.

2.1. WS operation

The REMS WS consists of a set of six boards distributed over two booms. At each boom, three of these boards are aligned with the axial direction of the boom and oriented at 120° with respect to each other (see Gómez-Elvira et al. (2012) and Newman et al. (2017)). As detailed in Domínguez et al. (2008), each board presents four hot dice, which are actively heated to maintain a constant temperature difference with respect to a reference (a fifth die) that is far enough from the others to be considered beyond any thermal interference (Fig. 1 shows an image of Boom 1 board 3 on Mars on sol 526). This approach is achieved through a first-order sigma-delta modulator. Each cubic die, which is 1.5 mm long and 0.4 mm high, has its own temperature sensor and heater and all are assumed to be thermally insulated from the boom structure through four Pyrex pillars with low thermal conductance. The temperature at each hot die is assumed to be uniform, with an estimated error of 0.5% at a temperature difference of 30 K with respect to the reference die (Kowalski et al., 2010). The purpose of this four-dice
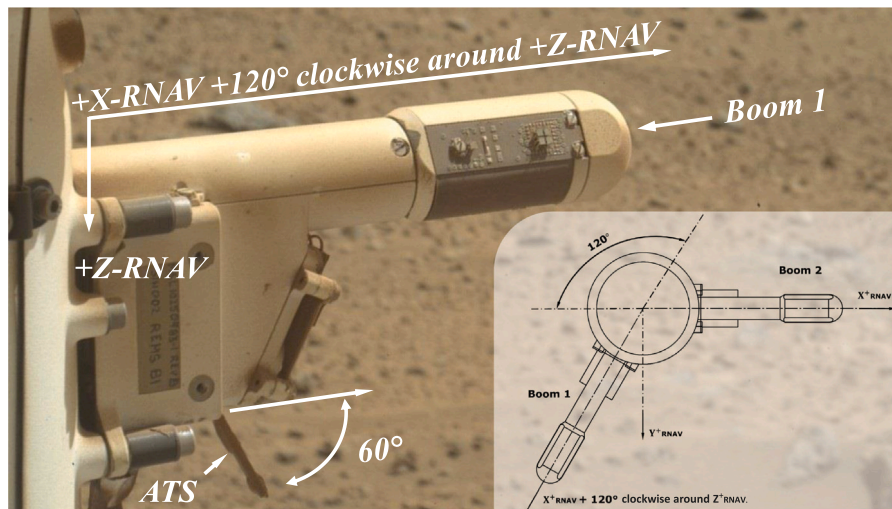
Fig. 1. Rover navigation frame over Boom 1 on the mast of the Curiosity rover on Mars, January 28th 2014, as seen by the Mars Hand Lens Imager (MAHLI) on sol 526. Boom 1 is 120° clockwise in $+Z_{RNAV}$ with respect to Boom 2, which points toward $+X_{RNAV}$. REMS Boom Image Credit: NASA/JPL-Caltech.

configuration is to monitor the assumed two-dimensional behavior of the forced convection that occurs over their squared surfaces (Gómez-Elvira et al., 2012), which are immersed in the thermal boundary layer of the booms. This measurement is performed by recording the required power to maintain a constant temperature difference for each die with respect to the reference. When combining the four signals, the systematic conduction losses to the structure can be removed (to the first order), which is critical in this approach. Radiation and conduction losses in the dice are calibrated for different power-injection scenarios and implemented as constants for all the dice (Gómez-Elvira et al., 2012).

By combining the four dice signals in pairs, two sinusoidal functions that are 90° phase-shifted and dependent on the angle of incidence of the in-plane airflow are obtained and converted to conductance along and across the four-dice setup. These two sinusoidal functions are characterized for each board under a certain wind regime and, later, the set of the three boards' combination obtained at each boom is implemented in an inverse model that correlates conductance values with a dimensionless Reynolds number, $Re = \rho \cdot v \cdot L_c / \mu$, across each boom. This number, traditionally used to describe flow regimes around obstacles, represents the ratio between the inertial forces and viscous forces of the airflow when surrounding the REMS booms. Depending on its value, a fluid flow can be classified as laminar or turbulent, and it depends on the fluid density ρ, the flow dynamic viscosity μ, the speed of the flow or wind speed v, and the characteristic length L_c; that is, the scale of the physical system considered.

The correlation between conductance and velocity is thus performed through the Reynolds number obtained from the inverse model, and the translation from Reynolds values to velocity vectors is determined through a mesh of experimental values that are measured in wind-tunnel facilities (Gómez-Elvira et al., 2012; Gómez-Elvira, 2013a,b,c). The local planar components of the longitudinal and cross conductance are then input parameters, and the output consists of the Reynolds number, which needs to be translated to wind speed values, the yaw angle ϕ (in the horizontal plane), and the pitch angle ψ (in the vertical plane). The wind-tunnel tests were performed in order to build a three-dimensional mesh of (Re, ϕ, ψ) values of $13 \times 18 \times 16$ points for the "low-speed" case; that is, for wind speeds $v \in [0, 20]$ m/s where greater resolution was desired, and $5 \times 18 \times 14$ points for the "high-speed" case, for wind speeds $v \in [25, 70]$ m/s. Each of these points corresponds to the longitudinal or cross conductance, G_{long} or G_{cross}, respectively, of one of the six REMS boards; thus, 12 hyper-surfaces $(Re, \phi, \psi, G_{long}$ or $G_{cross})$ are obtained.

A tessellation-based linear interpolation on these surfaces is applied to derive the final points (Re, ϕ, ψ) from each set of conductance values, and the final step implies a conversion from Reynolds numbers to wind speed values. The Reynolds number that is used for REMS is based on the diameter of the booms D; that is, the characteristic length assumed is $L_c \sim D = 30$ mm. Here, the booms are considered cylinders within an external and normal cross-flow. The air dynamic viscosity μ is modeled according to Sutherland's law (Newman et al., 2017), and the atmospheric density ρ is derived from both the ideal gas law and REMS pressure and temperature data. On Mars, the temperature required for the Reynolds and wind speed calculations is selected at each measurement as the lowest between the fluid temperature that is measured by the tip values of ATS Boom 1 and ATS Boom 2 (Gómez-Elvira, 2013c). If the collected differential thermal conductance data to be converted to wind speed and direction are too noisy, they are collected with voltages that are out of the established valid range or they present a gain that is not fully characterized, these data are removed by the WS, and not used for this conversion (Gómez-Elvira, 2013c). This situation is usually encountered during the night and its duration depends on the planetocentric solar longitude, which measures the position of Mars in its orbit around the Sun, as described in section 2.2.3 of Newman et al. (2017); that is, from ∼ 02:00 until approximately dawn around local summer solstice and from ∼ 20:00 until ∼ 08:00 around local winter solstice. Finally, velocity values are averaged every 5 min and angles are provided as the most frequent in these 5 min, and these data are then archived, quality labeled, and released in the PDS public base.

The instrument was calibrated in different wind-tunnel facilities in combination with a set of computational fluid dynamics (CFD) simulations to achieve a wind-sensing resolution of ±0.5 m/s for both vertical and horizontal speed and ±30° for the angles. Similarly, a wind-sensing accuracy of 1 m/s and 30° was targeted (Gómez-Elvira, 2013a,b,c). Most of the calibration tests were performed under ambient temperature conditions within the Mars Simulation Linear Tunnel (Gómez-Elvira et al., 2012) at the Center of Astrobiology (CSIC-INTA). In addition to this, the air temperatures introduced in the inverse model were not the minimum between those calculated from both ATS, as is done on Mars, but were recorded by an external sensor within the tunnel, and the range of wind speeds was not directly simulated over the REMS setup. Most importantly, to simulate representative Martian fluid regimes, the Reynolds number of the airflow provided by the tunnel was modified by changing the pressure, and thus the density, instead of the velocity.

The WS boards 2 and 3 in Boom 1 and board 1 in Boom 2 have not been operative since MSL landed. A possible explanation for this

issue was the impact of small rocks onto the boards while landing, although this possibility has not been confirmed (Newman et al., 2017). Thus, the on-ground calibrated wind retrieval algorithm, based on an inverse model that interpolates the solution on an experimental mesh of (Re, ϕ, ψ) values obtained from wind tunnel tests by measuring 12 sets of conductance values (a pair of G_{long} and G_{cross} values at each board), was no longer available. Instead, this mesh was reconstructed by combining only four conductance values, corresponding to the G_{long} and G_{cross} values on boards 2 and 3 from Boom 2, even though REMS was already on the surface of Mars. The final retrieval then relied on a system of less information than initially required. This must have produced an uncontrollable error, although the PDS maintained the originally defined error for the WS values. The retrieval also used the results of CFD studies performed with a fluid flow and heat transfer simulation software (EFDLab) over a representative geometry of the REMS booms and the Curiosity rover mast (RSM) and Mast Camera (MastCam). The purpose was to include the effect of the rover body (especially the RSM) on perturbing the airflow around the booms, to develop an algorithm that chooses the appropriate boom – the one least perturbed – from which to use the data. The placement of the two booms was designed such that at least one board would always be exposed to the free stream airflow on Mars' surface, outside the thermal or viscous wake of the RSM. However, because only boards 2 and 3 on a single boom (Boom 2) were used after landing to measure the velocity field, these boards were immersed in the viscous and thermal wake of the MSL platform for some rover orientations. Because of this, the WS wind direction retrieval range was also reduced. The WS retrieval algorithm provides "front" directions if the wind is coming from 0° to 90° and from 270° to 360° according to the Rover Navigation Frame (RNAV) (Kim et al., 2014) (see Fig. 1). Similarly, it provides "rear" directions if the wind is coming from 90° to 270°, with an associated error in this configuration of ±45°; that is, rear winds can only come from 135° (rear-right quadrant) or 225° (rear-left quadrant) according to the RNAV reference system. The final wind direction is provided as the most frequent value over 5 min of 1-Hz data. The WS retrieval algorithm provides wind directions with an error of ±7.5° if wind is coming from the hemisphere in front of the rover, and wind speeds may only be retrieved for front winds; hence no wind speed information is available for rear winds.

Because of the reduced WS field of view, research activities focused on wind acquisition required specific orientations of the rover with respect to the airflow. This operation was performed and prioritized, for example, during the Bagnold Dunes campaign (Newman et al., 2017). Only front winds were considered; that is, winds approaching the rover with a negative X_{RNAV} component according to the RNAV (Kim et al. (2014), see Fig. 1). Section 4 includes a complete geometrical description of both booms within the RNAV system. For these front winds, Newman et al. (2017) estimated an uncertainty of 20% without considering the effects of the rover body, which physically and thermally modifies the surrounding environment. The 5-min averages of the REMS WS data do not generally include values acquired for every second within that interval. These averages discard data packages that were produced with excessive electronic noise or rear wind measurements (Newman et al., 2017). Because of the natural underlying fluctuating nature of the winds during the given interval, it is unclear how the error is reduced or increased by averaging a 5-min sequence of partially filtered data. Finally, Boom 2 board 2 was reported to have failed on mission sol 1485, whereas Boom 2 board 3 failed on sol 1491. This implies that from sol 1491 (October 16th, 2016) to the present, no wind speed measurements have been recorded on the MSL mission.

2.2. ATS operation

The ATS consist of two thin rods of FR4 material, each attached to one of the REMS booms at the mast of the MSL Curiosity rover. Each rod has three bonded Minisens RTD Thermistors Pt1000 class A,

which provide temperature readings with an accuracy of 5 K and a resolution of ±0.1 K. These readings are at the base, T_b, where they are assumed to be equal to the base temperature of the booms; at an intermediate point, T_{Ln}; and at the tip of the rod, T_a (Gómez-Elvira et al., 2012). Each FR4 rod is 35 mm long and has a cross-section of 2 mm × 3 mm. The ATS are each mounted on a different boom, pointing to the surface with a 60° inclination angle with respect to the horizontal plane. Boom 2, its ATS rod, and the forward direction of the rover or "front direction" are contained within the vertical RNAV XZ plane, and Boom 1 and its ATS rod are contained within a vertical plane at 120° clockwise with respect to the RNAV XZ plane; that is, the plane formed when rotating the RNAV XZ-plane 120° around the positive RNAV Z-axis. Fig. 1 shows the ATS rod disposition along Boom 1 with respect to the RNAV reference frame. Temperatures are recorded at a rate of 1-Hz over the first 5 min of each hour for nominal acquisitions or during the entire hour for extended acquisitions (Newman et al., 2017). To obtain the temperature surrounding the ATS rods, the measuring principle is based on the energy-balance equation for the temperatures along each ATS rod, assuming local thermal equilibrium. This approach has been widely used for natural convection modeling around cylindrical rods with a high length to cross-section ratio and a base that is maintained at a constant heat flux and that usually raises its temperature to a constant value above the ambient conditions (Mueller and Abu-Mulaweh, 2006; Grunt et al., 2016). For these ratios, the temperature distribution is assumed to be uniform across the cross-section of the rods, and their length is high enough to ignore heat loss at the tip. Thus, we can reduce the heat transfer to a one-dimensional problem. For ATS temperature retrieval, we choose the approach by Mueller and Abu-Mulaweh (2006) to model the ATS rods, which are heated at their base. On Mars, the metallic base where the booms are attached can be hotter or colder than the air, depending on the time of day, but this method also works for the inverse thermal situation. A detailed description of the application of Mueller and Abu-Mulaweh (2006) for REMS ATS temperature retrieval is provided in Gómez-Elvira et al. (2012). This method is already used in REMS operations to give air temperatures at a frequency of 1-Hz; finally, the temperature data are archived and used later as temperature reference for the retrieval of the WS.

3. Materials and methods

The purpose of this section is to describe a retrieval algorithm that, using the same energy-balance equation applied to the REMS ATS temperature retrieval, may provide information about wind. The assumptions and modeling applied to this algorithm conception are detailed and justified here, with the results of the application of this method to Martian data shown in Section 4.

Section 3.1 describes the model upon which this retrieval is based and some preliminary wind tunnel results that suggest an existing correlation between the m-parameter (a dimensionless parameter that expresses the strength of the temperature gradient along the REMS ATS rods) and the unperturbed wind speed. This correlation exists because heat exchange and the heat transfer coefficient (which is directly related to the m-parameter) include natural and forced convection phenomena, and the latter depends directly on wind speed. As a result, if the heat transfer coefficient is properly modeled, wind data could be provided by estimating the m-parameter from the REMS ATS readings. Sections 3.2 and 3.3 are thus dedicated to finding the right modeling for the heat transfer coefficient. Section 3.2 details the assumptions for modeling the fluid flow around the REMS ATS rods in order to later develop, in Section 3.3, how the forced convection over the REMS ATS rods is modeled within this fluid flow. When modeling forced convection in this section, the averaged Nusselt number over the ATS rods is used to establish a correlation between wind speed and the averaged convective heat transfer coefficient. For this purpose, Section 3.3 details, in Sections 3.3.1 and 3.3.2, how the Nusselt number has been modeled in parallel and normal directions, respectively, with

respect to the ATS rods. Once the heat transfer coefficient was modeled through the Nusselt number for each REMS ATS rod, we added an additional correlation between both rods (Section 3.4) to obtain a system of equations that could provide wind speed and direction from REMS ATS temperature data. Next, Section 3.5 describes the testing of this system of equations in a representative geometrical model of the REMS booms configuration under Martian conditions through CFD simulations. Several theories were applicable when modeling the convective heat transfer coefficient around the ATS rods for normal flows, so CFD studies were performed to choose the model that best suits the heat transfer problem addressed. Finally, based on the results of Section 3.5, Section 3.6 details the final wind retrieval algorithm proposed to be applied to REMS ATS temperature data from the surface of Mars.

3.1. The m-parameter model

The wind retrieval algorithm is based on the correlation of the dimensionless averaged m-parameter, $\overline{m}$, from the ATS rods with the local wind speed; the value of $\overline{m}$ depends on the convective ($\overline{h}_c$) and radiative ($\overline{h}_r$) heat transfer coefficients, the former of which depends on local wind speed. For this retrieval, the energy-balance law was adapted from Mueller and Abu-Mulaweh (2006) to a rectangular cross-sectional cylinder. Thus, a different average m-parameter is obtained for each ATS rod by considering a differential lateral surface $dA_s = (2a + 2b) \cdot dx$ and a cross-section $A_c = a \cdot b$, where $a = 2$ mm and $b = 3$ mm (the side lengths of the ATS rectangular cross-section) and x is the longitudinal coordinate along the rod of length L starting at the base:

$$\overline{m} = L \cdot \sqrt{\frac{2 \cdot (a+b) \cdot \overline{h}}{\kappa_{ATS} \cdot a \cdot b}}.$$ (1)

Here, $\overline{h}$ is the averaged heat transfer coefficient considering both convection and radiation normal to the lateral surface of the ATS rods, $\overline{h} = \overline{h}_c + \overline{h}_r$; and κ_{ATS} is the thermal conductivity of the FR4 (of which the ATS rods are made of). κ_{ATS} is assumed to be 0.8 W/(m K) between the bonded Pt1000 thermistors, which constitutes a reasonable value for printed circuit board (PCB) glass-fiber laminates such as the ATS rods for the in-plane dimension; that is, in directions parallel to the laminates that conform the composite material of the rod-shaped PCB (Sarvar et al., 1990). This assumption is necessary because no measurements were performed for κ_{ATS} on the REMS ATS rods. As detailed in section 4.3 of Gómez-Elvira et al. (2012), the system used for the retrieval is as follows:

$$T_a - T_f = (T_b - T_f) \cdot \frac{1}{cosh[\overline{m}]}$$ (2)

$$T_{Ln} - T_f = (T_b - T_f) \cdot \frac{cosh[\overline{m} \cdot (1 - \frac{1}{n})]}{cosh[\overline{m}]},$$ (3)

where the fluid temperature T_f and the averaged dimensionless m-parameter $\overline{m}$ of each ATS rod can be retrieved. Here, the analytical solution for the boundary problem developed by Mueller and Abu-Mulaweh (2006) is applied at the tip of the ATS rods, $x = L$ (Eq. (2)), and at $x = L/n$; that is, where the intermediate Pt1000 of the rods is located (Eq. (3)). For both the REMS and HABIT ATS rods, the intermediate Pt1000 sensor that provides the T_{Ln} temperature readings is located at $x = L/4$; that is, $n = 4$ in Eq. (3). Because of the T_{Ln} sensor, the analytical solution of the Mueller and Abu-Mulaweh (2006) boundary problem can be applied twice, resulting in two equations with two unknowns: T_f and $\overline{m}$, as detailed in Gómez-Elvira et al. (2012). In fact, T_f and $\overline{m}$ are retrieved simultaneously as part of the existing REMS ATS data analysis; T_f is archived as data product, the air temperature, but so far $\overline{m}$, which contains useful information about the heat flux regime, has been discarded. Once $\overline{m}$ is calculated, the average heat transfer coefficient $\overline{h}$ can be retrieved (Eq. (1)). This coefficient combines the radiative and convective effects, where the latter is dependent on the natural and forced convection, and thus on the wind speed. As a

result, if the average convective heat transfer coefficient $\overline{h}_c$ is properly modeled when considering the forced convection terms because of the airflow around the ATS rods, the $\overline{m}$ parameter values can be correlated with the wind speed values. This is the purpose of this work; namely to demonstrate the usefulness of $\overline{m}$ to retrieve information about the wind. The wind retrieval concept is then based on the estimation of $\overline{m}$ for each rod and its subsequent correlation with the corresponding wind speed through the overall heat transfer coefficient $\overline{h} = \overline{h}_c + \overline{h}_r$.

To illustrate this principle, we tested the HABIT engineering model (EM) in a wind tunnel under terrestrial atmospheric conditions. These tests showed that the dimensionless m-parameter averaged over an ATS rod that is overheated at its base presents some correlation with wind speed when the airflow is normal to the rod (Fig. 2). As can be inferred from Eq. (1), this correlation is expected to be associated with the convective heat transfer coefficient term $\overline{h}_c$, and it must be modeled to be able to use m-parameter retrievals for estimation of wind speed.

The tests were run under ambient conditions: pressure $P = 1010.32$ mbar, temperature $T = 22.8$ °C, and relative humidity $RH = 41\%$. The HABIT container unit (CU; Fig. 2) was artificially heated to simulate the usual overheating of Mars exploration surface platforms because of the low ambient temperatures and the action of the heating systems that are required for the electronic components to survive. Three heaters (Vishay Series LTO50) were attached to an aluminum plate to which the HABIT CU was bolted. The heaters were each powered up through a bench power supply (RND 320-KA3305P) at 28 V, providing a heating power of 1.5 W that increased the temperature of the 78.5 g of aluminum 7075-T6 HABIT CU setup around 5 K above ambient conditions. This heating was maintained constant during the wind tunnel tests because its purpose was to simulate a passive heating source, such as the ExoMars surface platform, which can be assumed to be constant for a 1-h test. The samples were recorded at 1 Hz and later averaged every 10 s.

To create a reference of the airflow temperature and wind speed for comparison with the retrieval, a commercial wind sensor ComfortSense®-Mini 54N95 with a T33 probe was used together with a NI cDAQ-9178 rack and a 16-bit analog-to-digital converter NI-9215 from National Instruments®. The T33 probe is an omnidirectional thin film sensor that measures both wind speed and temperature. It consists of a quartz sphere 3 mm in diameter coated with a thin film of nickel and refrigerated when immersed in an airflow. The probe measures the energy needed to maintain the temperature difference between this sphere and a replica, which is later translated into wind speed measurements through a calibrated voltage to wind speed function. This setup provided reference readings with 5% accuracy in speed and 0.2-K accuracy in temperatures for wind speeds ranging from 0 to 5 m/s.

The Reynolds numbers under Earth's ambient conditions over the HABIT ATS rods are almost two orders of magnitude higher than the expected values on the surface of Mars for the same setup. This changes the heat exchange scenario considerably, in addition to the radiation terms. For these reasons, the available AF1300 wind tunnel was not used to validate the HABIT ATS retrieval performance, but the m-parameter model concept as a proxy for wind speed retrieval. The validation of the correlation between the m-parameter and wind speed values should be only performed at a testing facility that provides Martian surface conditions or, in the absence of these, by using the wind dataset from Mars, which would be assumed the reference because its data are already validated under Martian conditions. In this work, we validated the concept with the existing Mars measurements from the REMS WS. Future work will report the true calibration of this method in wind tunnel tests that are currently being developed for the HABIT instrument under Martian conditions.

As shown in Fig. 2, the m-parameter followed the wind speed pattern. The wind pattern over the setup was set manually to different wind speeds, $v \in [0, 2.5]$ m/s, to observe convergence to a value of the HABIT EM ATS rod m-parameter calculations at different wind speeds; that is, when reaching a new equilibrium condition coming
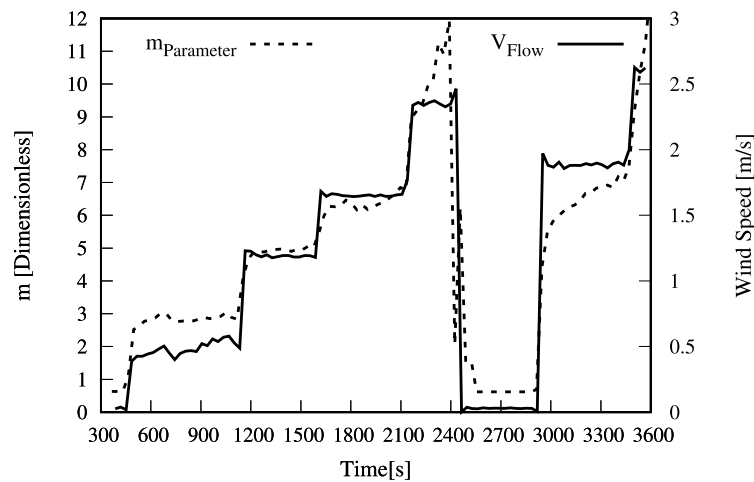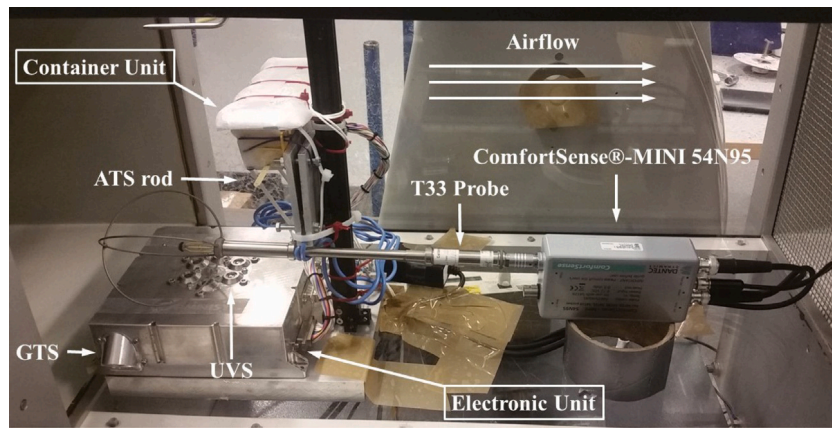
Fig. 2. (Above) HABIT EM and ComfortSense®-Mini 54N95 T33 probe within the test chamber of the Luleå University of Technology subsonic AF1300 wind tunnel. (Below) Ten-second averages of wind speed measured by the ComfortSense®-Mini 54N95 T33 probe (V_{Flow}) and retrieved m-parameter from the 3 temperature sensors along the left ATS rod with respect to the incoming frontal wind speed; that is, when the airflow is normal to the rod, at $P = 1010.32$ mbar, $T = 22.8$ °C, and relative humidity $RH = 41\%$.

from a lower or higher wind speed case. In this test, the ATS rod could exchange heat with the ambient air through conduction, radiation, and convection, although convection was dominant in this case because of the ambient conditions in terms of pressure and temperature. For the airflows tested in the tunnel, the dominant heat transfer mechanism for the rod was forced convection. This mechanism involves the presence of relative movement between the solid body and the gas at the interface of the media. When the wind speed is reduced in the tunnel, the rod is expected to evacuate less heat through forced convection. This is because the local wind speed around the ATS rod decreases, which in turn increases the absolute temperature readings at each Pt1000 sensor and modifies the temperature profile along the rod. When the wind speed is increased in the tunnel, the cooling performed by forced convection over the overheated ATS rods is expected to increase, reducing the overall absolute temperatures measured by each Pt1000 and modifying the temperature cooling profile along the rod. As can be observed in Eqs. (2) and (3), the system that provides the m-parameter depends on the temperature difference between Pt1000 readings (i.e., the temperature gradient) and not on absolute temperatures if all of the temperature values increase or decrease by the same amount. We see in Fig. 2 that the m-parameter values at the start of the test, $t \in [350, 450]$ s, and after the first maximum in speed, $t \in [2500, 2900]$ s, are similar, even though in the latter the instrument was previously working under a 10 m/s airflow. Even though the temperatures collected by each Pt1000 may differ in absolute terms in both cases because of the higher cooling of the CU structure originated during the 2.5 m/s stage, the ratio between temperature readings was similar, and so was the m-parameter value.

Note that the output of the m-parameter model is affected by the electronic noise of the HABIT EM. In addition to this, the Pt1000 sensors attached to the ATS rods of the HABIT EM are exposed to external airflow, and not encapsulated between two layers of FR4 as occurs in the REMS ATS or HABIT flight model (FM) ATS rods. This makes the Pt1000 readings more sensitive to wind oscillations than the REMS ATS temperature readings, especially when exposed to airflows at Earth's densities under atmospheric sea-level conditions.

For the periods $t \in [2100, 2400]$ s, $t \in [3500, 3600]$ s, and $t \in [3000, 3400]$ s, the estimation of the m-parameter value changes, even though the wind speed of the tunnel is set to a constant value. Because the wind speed in the wind tunnel was set to values $\gtrsim 1.5$ m/s for these cases, it is possible that this airflow regime created some vibrations on the rod structure. The HABIT EM ATS rods were not designed to operate under these wind speed values at ambient atmospheric densities on Earth, and the attachment of the ATS rods to the HABIT structure is not meant to handle such aerodynamic drag. Furthermore, the higher heat transfer rates on Earth than on Mars at the speeds observed in these periods appear to be strong enough to cool the overheated CU metallic structure. The greater thermal inertia of the CU with respect to the ATS rods makes the system converge more slowly (~ 300 s) to the new equilibrium condition when increasing the speed to values $\gtrsim 1.5$ m/s. The longer response time is particularly evident for the change in wind speed from 0 to 1.5 m/s at $t \sim 2900$ s. As a result, because the equilibration time for the ATS in Martian conditions is found to be 20 to 80 s (Gómez-Elvira et al., 2014), any longer response times evident in Fig. 2 may be due to the larger changes in Reynolds numbers on Earth

than on Mars and the thermal inertia of the full structure. It is for these reasons that no higher velocities had to be tested in the tunnel.

In summary, the tests with the HABIT EM in the AF1300 wind tunnel were performed to illustrate the expected, yet unknown, correlation between the m-parameter and wind speed, and whose modeling is developed in Sections 3.2 and 3.3. The ultimate validation of this retrieval concept would rely instead on comparison with the REMS WS wind measurements, which present a specific measurement error in wind speed and orientation for 5-min averages, as discussed in Section 4.

3.2. Fluid model

To illustrate the retrieval, we modeled the atmospheric conditions within the Martian thermal boundary layer at 1.5 m over the surface and the forced convection around REMS ATS rods as follows. Air was assumed to be a continuous fluid when applying the Navier–Stokes equations. This assumption implies that the validity range of this analysis is constrained to a Knudsen number $k_n = \lambda_f / L_c < 0.1$ (Schoenenberger et al., 2005; Murri, 2010), where L_c corresponds to the characteristic length and λ_f to the mean free path between molecules of the Martian atmosphere. The latter is defined as follows:

$$\lambda_f = \frac{k_B T}{\sqrt{2}\pi D_{gas}^2 P},$$ (4)

where k_B is the Boltzmann constant, T the air temperature, P the air pressure, and D_{gas} the kinetic diameter of the gas considered; that is, the size assumed for the molecules of the Martian atmosphere. The minimum scales to which the results would be consistent with the fluid-continuity hypothesis would range from $L_{min} \sim 3.9 \cdot 10^{-5}$ to $L_{min} \sim 8.8 \cdot 10^{-5}$ m for a simplified CO_2 atmosphere, depending on the average pressure and temperature seasonal oscillations, always within the ranges $P \in [700, 1000]$ Pa and $T \in [180, 280]$ K, respectively, as measured by MSL at Gale Crater (Martínez et al., 2017b). The kinetic diameter has been assumed $D_{gas} = D_{CO_2} = 3.94 \cdot 10^{-10}$ m according to Ismail et al. (2015). The minimum scale considered in the modeling was the characteristic length of the cross-section of each ATS rod $L_{cross} = 3 \cdot 10^{-3}$. Because $L_{min}/L_{cross} \sim 10^{-2}$, the atmosphere was considered a continuous fluid and the ideal gas law was assumed. The molecular weight was assumed to be 43.49 g/mol, corresponding to 2.7 mol %N_2, 1.6 mol %Ar, and 0.15 mol %O_2 (Seiff and Kirk, 1977). The dynamic viscosity and conductivity of the fluid, $\mu_f (T)$ and $k_f (T)$, were modeled following the Sunderland's temperature-dependent kinetic theory approach for a low-density CO_2 atmosphere and for temperatures $T \in [190, 1700]$ K for $\mu_f (T)$ and $T \in [180, 700]$ K for $k_f (T)$, with an error estimation of $\pm 2\%$ for the mentioned temperature ranges (White, 2011):

$$\frac{\mu_f}{\mu_{f0}} \approx \left(\frac{T}{T_0}\right)^{3/2} \frac{T_0 + S_{\mu_{CO_2}}}{T + S_{\mu_{CO_2}}},$$ (5)

$$\frac{k_f}{k_{f0}} \approx \left(\frac{T}{T_0}\right)^{3/2} \frac{T_0 + S_{k_{CO_2}}}{T + S_{k_{CO_2}}},$$ (6)

where $\mu_{f0} = 1.370 \cdot 10^{-5}$ N·s/m^2 and $k_{f0} = 0.0146$ W/(m · K) correspond to the dynamic viscosity and thermal conductivity, respectively, of CO_2 at $T_0 = 273$ K; and $S_{\mu_{CO_2}} = 222$ K and $S_{k_{CO_2}} = 1800$ K correspond to the CO_2 Sutherland constants; that is, the effective temperatures tabulated for each gas. The specific heat, $C_p(T)$, was modeled following the temperature-dependent polynomial expression for a low-pressure regime ($P < 1 \ bar$) and temperatures $T \in [200, 3500]$ K (Kee et al., 2000):

$$\frac{C_p(T)}{R} = a_1 + a_2 \cdot T + a_3 \cdot T^2 + a_4 \cdot T^3 + a_5 \cdot T^5,$$ (7)

where R is the universal gas constant and the coefficients [a_1, a_2, a_3, a_4, a_5] = [3.85746029, $4.41437026 \cdot 10^{-3}$, $-2.21481404 \cdot 10^{-6}$, $2.45919022 \cdot 10^{-9}$,

$-1.43699548 \cdot 10^{-13}$]. For temperatures $T < 200$ K, $C_p(T)$ was assumed to vary linearly and the values were extrapolated.

To properly model the expected fluid regime around the ATS rods, the compressibility and Reynolds number range were estimated by using REMS measurements from Gale Crater (Gómez-Elvira, 2013b). Depending on the magnitude of the Reynolds number, the fluid regime could belong to the laminar region, the turbulent region, or a transition between them, which would determine the heat transfer equations to be chosen when modeling the forced convection mechanism in Section 3.3. The Reynolds number that sets the transition from laminar to turbulent flow around an obstacle is called the critical Reynolds number, Re_{cr}.

For the considered length scales, the flow was assumed to be incompressible; the Mach number is $M \sim 1 \cdot 10^{-3}$ for the nominal range of pressures and temperatures in Gale Crater and for a modeled CO_2 atmosphere. On the other hand, the Reynolds number for the widest expected wind speed range according to Viúdez-Moreiras et al. (2019b) and based on the longest cross-sectional characteristic length $L_c = 3.6 \cdot 10^{-3}$ m was $5 < Re < 120$. It should be noted that for the wind speed range considered, peak wind speeds may have exceeded the average speeds that were released as reliable.

Although the critical Reynolds number for circular cylinders in cross-flow presents a wide agreement with $Re_{cr} \sim 10^5$ (Achenbach, 1971), this value differs extensively from that for rectangular cylinder scenarios, where no clear limit exists for the transition from laminar to turbulent flow. Experimental and numerical simulations at low Reynolds numbers have been performed for this flow region, providing values of $Re_{cr} \sim 40$, although the width-to-height ratio, D/H, of the rectangular cylinder cross-section has been demonstrated to affect the appearance of this transition, with $Re_{cr} \sim 500$ for $D/H = 2$ and $Re_{cr} \sim 10^3$ for $D/H = 3$ (Okajima, 1982).

The wind speed observed on the Martian surface by REMS WS was usually on the order of $v \lesssim 10$ m/s, corresponding to $Re \lesssim 38$. In addition, transition studies did not consider the angle of incidence of the flow over the rectangular cross-section, which is expected to reduce its bluff shape. Thus, this model does not consider possible transition to turbulent flow, and laminar incompressible flow is assumed. This means that the turbulence intrinsic to the atmosphere is considered negligible in the retrieval.

3.3. Forced convection around ATS rods

To model the forced convection around the ATS rods and establish a correlation between the convective heat transfer coefficient and the wind speed, we modeled the average Nusselt number (Nu) at each rod within this laminar incompressible flow. This number represents a ratio between the convective and conductive heat transfer terms within the flow around the rods, which is defined as $Nu = \overline{h}_c L_c / k_f$. Here, $\overline{h}_c$ is the average convective heat transfer coefficient. Numerous previous studies focused on this forced convection modeling over cylinders, including curvature effects and skin-friction deviations, although not as many studies considered cylinders with a rectangular cross-section. The Nusselt number in this study was developed for a rod assumed to be a cylindrical body of $D = 2.76 \cdot 10^{-3}$ m and a length-to-diameter ratio, L/D, of ~ 12. This cylinder, however, is always exposed to both axial and cross-flow; therefore, the total average Nusselt number should consider the effect of the angle of incidence of the flow with respect to the axial direction of the cylinder, β. Oosthuizen and Mansingh (1986) experimentally studied the average Nusselt number of "short" cylinders that were immersed in flow with different angles of incidence and proposed an empirical correlation that considers the Nusselt numbers both across and along these cylinders for different L/D ratios. Thus, we can correlate the angle of incidence β with the total forced convection that acts over the cylinders. An experimental correlation (8) is obtained for L/D ratios from 0 to 12:

$$Nu/Nu_{Dh} = f(Nu_{Dv}/Nu_{Dh}),$$ (8)

where Nu_{Dh} represents the Nusselt number if only the forced convection parallel to the cylinder is relevant, and Nu_{Dv} applies if only the normal forced convection over the cylinder is important. Consequently, both Nusselt numbers are assumed to follow the relationships (9) and (10):

$$Nu_{Dh} = Nu_{D_{0°}} \cdot [cos(\beta)]^{0.25} \tag{9}$$

$$Nu_{Dv} = Nu_{D_{90°}} \cdot [sin(\beta)]^{0.25}. \tag{10}$$

Here, $Nu_{D_{0°}}$ and $Nu_{D_{90°}}$ represent the Nusselt numbers at an angle of incidence of $\beta = 0°$ and $\beta = 90°$, respectively. Finally, an experimental correlation was provided by Oosthuizen and Mansingh (1986) for the total average Nusselt number over the cylinders depending on the ratio L/D, which we approximated according to their results for $L/D = 12.62$ as Eq. (11):

$$Nu = Nu_{Dv} + Nu_{Dh}. \tag{11}$$

Because, according to Section 3.1, the modeling of the m-parameter only considers convective heat transfer normal to the rods, the axial contribution to the overall forced convection is removed from the total average convective heat transfer coefficient. Eq. (12) is proposed for the average convective heat transfer coefficient $\overline{h}_c$ over the ATS rods following an equivalent reasoning to that of Mueller and Abu-Mulaweh (2006):

$$\overline{h}_c = \frac{\overline{m}^2 \cdot k_{ATS} \cdot a \cdot b}{L^2 \cdot 2 \cdot (a+b)} - \overbrace{\sigma\epsilon(T_s^2 + T_\infty^2)(T_s + T_\infty)}^{\text{Radiative heat transfer coefficient } \overline{h}_r}$$
$$= \frac{k_f}{Lc_v} \cdot Nu_{D_v} - \frac{k_f}{Lc_h} \cdot Nu_{D_h}. \tag{12}$$

In Eq. (12), T_s represents the surface temperature of the ATS rods, which is modeled as the average of the 3 Pt1000 measurements, $T_s \approx (T_a + T_{Ln} + T_b)/3$. Similarly, T_∞ is the fluid temperature at infinity as perceived from the ATS rods, considering the scale of the characteristic length L_c chosen, the diagonal of the rod's rectangular cross-section $L_c \sim 3.6 \cdot 10^{-3}$ m for Nu_{D_v}, and the length of the rod $L_c \sim 3.5 \cdot 10^{-2}$ m for Nu_{D_h}. Additionally, the estimated fluid temperature is assumed similar to the value at infinity as seen by the characteristic length scale, $T_\infty \approx T_f$.

3.3.1. Axial-flow nusselt approach

The axial Nusselt distribution along a cylinder under laminar incompressible flow has been extensively studied (Na and Pop, 1996; Seban, 1951; Kelly, 1954; Glauert and Lighthill, 1955; Stewartson, 1955; Jaffe and Okamura, 1968; Cabeci, 1970; Curie, 1980; Lin and Shih, 1980; Sawchuck and Zamir, 1992; Sakiadis, 1961; Rotte and Beek, 1969; Karnis and Pechoc, 1978; Choi, 1982; Eswara and Nath, 1992). In particular, Beese and Gersten (1979) proposed a Nusselt distribution for cylinders within laminar incompressible flow, providing a solution for Navier–Stokes equations as an asymptotic expansion with respect to the perturbation parameter $\epsilon = 1/\sqrt{(Re_R)}$. Here, Re_R is the Reynolds number based on the radius of the cylinder. In this case, the approach considers the second-order effects of the curvature of the cylinder on the viscous and thermal boundary layers, which depend on the Prandtl number, Pr. This number is defined as the ratio between the viscous and thermal diffusive terms within the fluid flow around a body: $Pr = \mu C_p / k_f$. Although the ATS rods are modeled as cylinders and, thus, would not present a specific curvature, the removal of the additional terms would leave the Nusselt approach similar to one that corresponds to a plate, which is a far poorer approximation than the cylindrical approach. The strong assumption of the ATS rectangular-based rods as cylinders represents an intrinsic source of errors in the retrieval. After numerically integrating both the inner and outer asymptotic solutions for the boundary layer with several representative Prandtl values, for

$Pr = 0.7$ (model's Prandtl order of magnitude) the average Nusselt number along the ATS rods is assumed to be

$$\overline{Nu}_{D_h} = \overbrace{0.349 \cdot \sqrt{Re_{L/R}}}^{1^{st}\text{order}} + \overbrace{\underbrace{0.366 \cdot \frac{L}{R}}_{\text{Curvature}} + \underbrace{\sqrt{\frac{L}{R}} \cdot \theta'_{23}(L/R, 0, Pr)}_{\text{Interaction}}}^{2^{nd}\text{order}}, \tag{13}$$

where $Re_{L/R}$ is a dimensionless number based on the dimensionless ratio L/R, and θ'_{23} is the dimensionless interactive term resulting from the integration of the asymptotic solutions for the ratio L/R and $Pr = 0.7$.

The effects of the curvature of a cylinder over the surrounding flow are considered with the second-order terms, one for the curvature and the other to represent the interaction between the pure curvature terms and the first-order approximation, which depends on the Prandtl number, the ratio L/R, and the dimensionless scaled distance from the wall to the external flow. The defined scale is small enough to consider this limit to be infinity. This last term, $\sqrt{\frac{L}{R}} \cdot \theta'_{23}(L/R, 0, Pr)$, must be integrated for every Prandtl number, which could not be performed with the retrieval process that is proposed here based on 3 temperature measurements. The order of magnitude of the interaction terms is at least "Interaction" $\sim 4 \cdot 10^{-2}$ (Beese and Gersten, 1979) and, for the expected flow regime, the Prandtl number is $Pr \sim 0.7$. As a result, the term is assumed to be constant for $Pr = 0.7$ in this retrieval; therefore $\sqrt{\frac{L}{R}} \cdot \theta'_{23}(L/R, 0, 0.7) = 0.19$.

3.3.2. Cross-flow Nusselt approach

The Nusselt number for a cylinder that is immersed in a cross-flow was also extensively studied for low Reynolds regimes and rarefied gases, most of which were based on changes in the Reynolds and Prandtl numbers with the transport parameters. Some previous studies were focused in the Nusselt distribution over squared-based cylinders (Kalendar and Oosthuizen, 2013); however, we found no relevant work for the Re and Pr flow regime considered in our heat transfer problem. Therefore, as for the axial Nusselt modeling, the ATS rods here were assumed to be cylinders as well. This implies an additional source of errors in the retrieval. The correlations found were developed for certain margins of Re and Pr and adapted to meet the requirements at a specific range of (Re, Pr). Although most of these correlations were experimentally measured by using liquids, their agreement was not fully clear for different (Re, Pr) regimes (Sanitjai and Goldstein, 2004). Some of these approaches were tested to establish the best method for the model. In particular, the empirical expressions for forced convection that were proposed by McAdams (1954), Whitaker (Van Der Hegge Zijnen, 1956), Fand and Keswani (1972), and Perkins and Leppert (1964) were studied here because their operational ranges encompass the expected range for Mars. These expressions are detailed in Table 1, and the variations in the Nusselt number expressions for representative environmental and wind speed conditions at Gale Crater are shown in Fig. 3. The expected Reynolds and wind speed ranges are highlighted for these atmospheric conditions. As can be seen in Fig. 3, the average Nusselt variation with the Reynolds number does not show clear uniqueness for the expected window of wind speeds; that is, each model presents a different Reynolds number (and thus a different wind speed) for the same Nusselt number value. As a result, a CFD study under representative Martian conditions was used to determine which model best fits the expected fluid flow. Section 3.5 details the results of this study.

3.4. Closure of the retrieval algorithm

We next include an additional equation so that we have the same number of equations and unknowns when solving the retrieval algorithm. This was achieved by establishing a relationship between
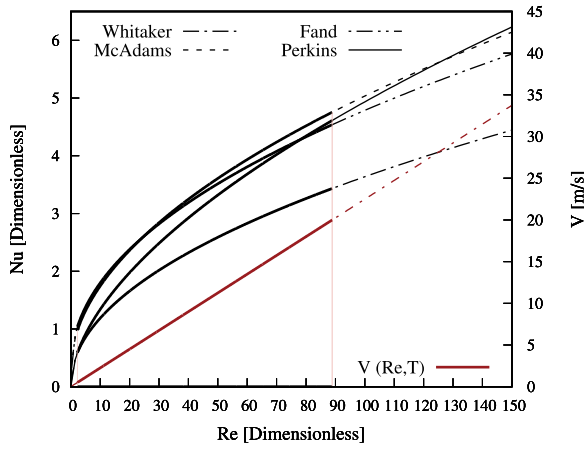
Fig. 3. Variation in the Nusselt number (Nu) as proposed by McAdams (1954), Whitaker Van Der Hegge Zijnen (1956), Fand and Keswani (1972), and Perkins and Leppert (1964) with respect to a Reynolds number (Re) based on $D = 2.76 \cdot 10^{-3}$ m for the atmospheric conditions of the MSL mission sol 730 averaged between 19:30 and 19:40: $P = 765.82$ Pa and $T_f = 225$ K. The highlighted values correspond to the expected velocity field and Mars conditions and the subsequent Re and Nu values.

Table 1
Nusselt empirical approximations Nu_{Dv} represented in Fig. 3 (McAdams, 1954; Van Der Hegge Zijnen, 1956; Fand and Keswani, 1972; Perkins and Leppert, 1964).

Author	Re_D range	Average Nusselt approximation
McAdams (1954)	$[1, 10^5]$	$Nu_{Dv} = (0.4Re^{0.5} + 0.06Re^{2/3})Pr^{0.4}(\mu_f/\mu_s)^{0.25}$
Whitaker (1956)	$[0.1, 10^3]$	$Nu_{Dv} = 0.32 + 0.43Re^{0.52}Pr^{1/3}$
Fand (1972)	$[0.01, 2 \cdot 10^5]$	$Nu_{Dv} = 0.184 + 0.324Re^{0.5} + 0.291Re^n$
		$n = 0.247 + 0.0407Re^{0.168}$
Perkins (1964)	$[40, 10^5]$	$Nu_{Dv} = (0.31Re^{0.5} + 0.11Re^{0.67})Pr^{0.4}(\mu_s/\mu_f)^{0.25}$

the ATS rods. The system can be thus solved when applied to the temperatures measured at the ATS rods of the CFD study.

By neglecting the vertical component of wind over the REMS structure, the system of Eqs. (2), (3), (9), (10), (11), (12), and (13) provides a model of the forced convection around each ATS rod, which depends on the external horizontal wind speed and angle of incidence $Nu = f(V_h, \alpha)$. This α angle is defined in the horizontal plane from Boom 2 to Boom 1; that is, any horizontal wind vector between booms would be at $\alpha°$ with respect to Boom 2 and at $\alpha° - 120°$ with respect to Boom 1.

By introducing the equation for the axial Nusselt number (Eq. (13)) and the equation for one of the models corresponding to the cross-flow Nusselt number listed in Table 1 into Eq. (12), together with the definition of the Reynolds number, we obtained an expression at each ATS rod with two unknowns: $V = f(V_{Boom1}, \alpha)$ for the ATS rod of Boom 1 and $V = f(V_{Boom2}, \alpha)$ for the ATS rod of Boom 2. V_{Boom1} and V_{Boom2} correspond to the component of the horizontal wind speed vector when projected normal to the ATS rods of Boom 1 and Boom 2, respectively; that is, the wind speed that the m-parameter perceives at each ATS rod (as explained in Sections 3.1 and 3.3). Thus, the application of these equations to each ATS rod results in a system of two equations with three unknowns. To close this problem, a geometrical relationship between the projections of the horizontal velocity vector normal to each ATS rod is proposed in Eq. (14). In this expression, the temperature profile at each ATS rod is assumed to be shaped only by forced convection because of a unique horizontal wind velocity field $\overline{V}_h$. A detailed view of the geometry of the problem is represented in Fig. 4.

$$\frac{V_{Boom2}}{V_{Boom1}} = \frac{V_h \cdot sin(\beta)}{V_h \cdot sin(\gamma)} = \frac{V_h \cdot sin[acos[cos(\alpha) \cdot sin(30°)]]}{V_h \cdot sin[acos[cos(120° - \alpha) \cdot sin(30°)]]} \quad (14)$$

The velocity field is represented by horizontal vectors $\overline{V}_h$ that describe an angle α with respect to Boom 2 axis $\equiv X_{RNAV}^+$, which

is positive clockwise from Boom 2 to Boom 1. Because of the actual geometry of the problem, Eq. (14) can only be applied to a certain range of $(V_{Boom2}/V_{Boom1}, \alpha)$ to provide a system with a unique solution. As a result, $\alpha \in [12.95°, 107.05°]$ for $V_{Boom2}/V_{Boom1} \in [0.88, 1.13]$. Fig. 5 shows the validity region between the two booms. Other configurations of the ATS in different platforms would require a minor modification to this geometrical term.

It should be noted that both ATS rods were assumed to be under the same forced convection conditions; however, Boom 2 was 5 cm higher than Boom 1. Thus, the temperature of Boom 1 at its base is expected to be higher under similar wind conditions than that of Boom 2, which can change the shape of the temperature profile along ATS rod 1 with respect to ATS rod 2. It is worth noting that HABIT will have all three of its ATS rods attached in the same horizontal plane.

3.5. Cross-flow nusselt modeling selection

Because of the differences in the existing literature for the cross-flow Nusselt modeling stated in Fig. 3, a study is required that provides, under the same conditions, a comparative analysis of each of them when included in the system of equations developed in Section 3.4. The expressions provided by McAdams (1954), Van Der Hegge Zijnen (1956), Fand and Keswani (1972), and Perkins and Leppert (1964) were evaluated for the expected (Re, Pr) regime under the surface conditions of Mars through representative three-dimensional CFD studies over a geometry model for REMS booms with the ANSYS-Fluent® software. The main purpose of this analysis was to choose the best hypothesis for the cross-flow Nusselt modeling when retrieving both the wind speed and direction, assuming the ATS rods as cylinders. The application of the chosen cross-flow Nusselt modeling hypothesis to the complete retrieval algorithm was validated by comparing the retrieval results with actual wind data from the surface of Mars.

Fig. 4 shows the geometry model implemented for the simulation of forced convection around the ATS rods on the MSL rover. It consists on a mast 1 m long accommodated on top of a simulated 2.5 m × 2.2 m × 0.2 m rover deck. According to the CFD studies for the REMS WS calibration (Gómez-Elvira et al., 2012), Boom 2 is attached to the mast with its axis at a height of 39.3 cm with respect to the deck upper surface, Boom 1 is located 5 cm lower and at 120° with respect to the Boom 2 axis in the horizontal plane, and both booms are modeled according to their actual dimensions. The control volume defined for the CFD simulations is 10 m × 10 m × 10 m, where the structure was located at a height from the ground so the Boom 2 axis is at 1.5 m from the Martian surface.

This analysis focused on a representative environment at Gale Crater as recorded by REMS. In particular, the conditions were set for MSL sol 730 and averaged between 19:30 and 19:40. The temperature at the platform as recorded by the REMS UVS was set to 241 K, the air temperature to 225 K, and the ground temperature to 223 K. Nighttime conditions were chosen to avoid the limited capabilities of ANSYS-Fluent® when modeling infrared and solar radiation. However, the m-parameter model presented here for the airflow around the ATS rods does not, in any case, consider direct solar radiation incidence. This phenomenon creates strong local heating on the rods and modifies the thermal profile along their structure, which could bias the correlation between the average m-parameter and the wind speed. Consequently, nighttime conditions are preferred for this CFD analysis. It should be noted that removal of the radiation within the CFD analysis did not affect the Nusselt selection study; that is, the radiation term is common to all models and facilitated convergence of the solution. Thus, the $\overline{h}_r$ term corresponding to the radiative heat transfer between the ATS rods and the environment was omitted in Eq. (12) for the simulations in order to be coherent with the simplified physics modeled in the simulation when calculating the wind speed and direction. The wind orientation was set to $\alpha = 60°$ to force the same incidence of the flow over both ATS rods and provide an estimation of the expected error
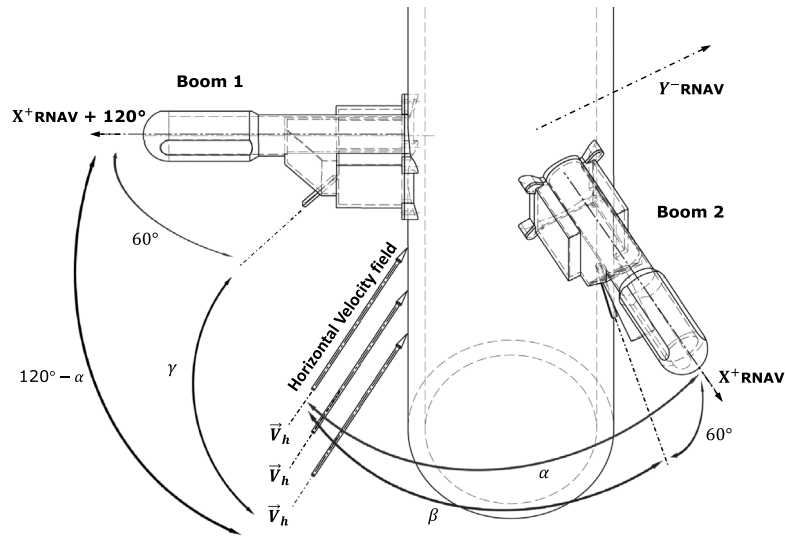
Fig. 4. Geometry of REMS angles implemented in the algorithm to retrieve both the horizontal wind speed and direction ($|\overline{V}_h|, \alpha$) from temperature distributions. β and γ correspond to the real angles that the horizontal wind speed vector forms with ATS rod from Boom 2 and Boom 1, respectively. These angles are measured by including both the $\overline{V}_h$ vector and the cylinder axis that models each ATS rod in the same plane. In these two planes, V_{Boom1} would be the normal projection of the horizontal wind-speed vector to ATS rod from Boom 1, and similarly V_{Boom2} to ATS rod from Boom 2. Their representation has been omitted for clarity.
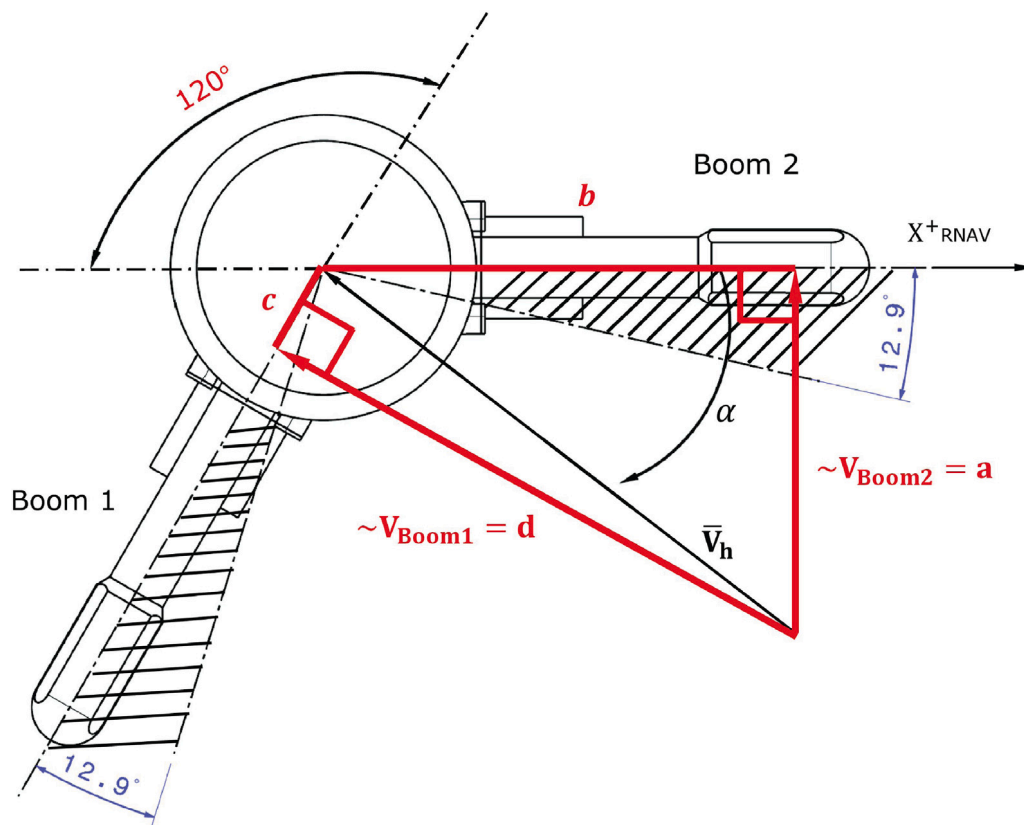

Fig. 5. Validity range of Eq. (14) for angle α in the horizontal plane: $\alpha \in [12.95°, 107.05°]$ for $V_{Boom2}/V_{Boom1} \in [0.88, 1.13]$. The striped area shows the small region between the booms that is outside this valid region. A horizontal velocity vector $\overline{V}_h$ within the admissible region for the wind speed and direction retrieval is included as an example. The angle α corresponding to $\overline{V}_h$ is also included. The red geometry scheme corresponds to the proposed "coarse" retrieval applied to the example velocity vector $\overline{V}_h$, as explained in detail in Section 3.5.1. (For interpretation of the references to color in this figure legend, the reader is referred to the web version of this article.)

under the assumption that both ATS rods are subjected to the same forced convection regime under similar conditions.

The application of Eqs. (2) to (14) to the set of temperature data that were measured at each ATS rod; that is, $(T_b, T_{Ln}, T_a)_{ATS1}$ and $(T_b, T_{Ln}, T_a)_{ATS2}$, results in a system of two non-linear equations with two unknowns. Each of these equations is the result of introducing the

Nusselt models and the definition of Reynolds number into Eq. (12) at each ATS. Thus, each expression would present as unknowns (V_{Boom1}, α) and (V_{Boom2}, α) for ATS from Boom 1 and ATS from Boom 2, respectively. By using the geometrical constraint provided in Eq. (14), the two expressions can be expressed as a function of (V_{Boom1}, α) or, alternatively, (V_{Boom2}, α). Once the system is solved, V_{Boom1} or V_{Boom2}
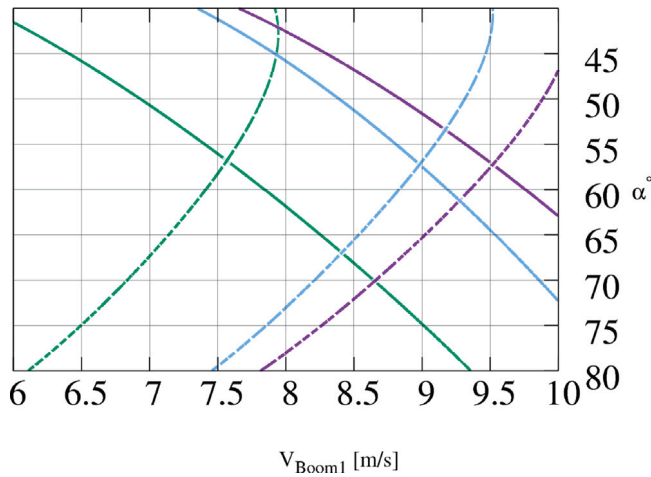
Fig. 6. Curves of solutions for each of the two non-linear equations for the $V = 8$ m/s case resulting from the intersection of both F1 and F2 solution fields with F = 0. In this plane, a solution is found in the common intersection of the pair of solution curves for each Nusselt theory; that is, at the intersection where $F_1 = 0$ and $F_2 = 0$. The solutions for the forced convection approach of Fand (green), Whitaker (purple), and Perkins (cyan) are shown, whereas the exact solution is located at $\alpha = 60°$. (For interpretation of the references to color in this figure legend, the reader is referred to the web version of this article.)

is calculated by using Eq. (14), where the true incidence angle is $\beta = acos[cos(\alpha) \cdot sin(30°)]$ and the final horizontal velocity module is $|\overline{V}_h| = V_{Boom2}/sin(\beta)$.

A battery of tests at different wind speeds were simulated for this orientation. V_{Inlet} refers to the wind speed value selected for the velocity field at the entrance of the control volume in which the setup composed of the REMS booms, the mast, and the rover deck are immersed in. The results for the approximation proposed by Fand and Keswani (1972) are listed in Table 2. In this table, the results when solving the Eqs. (2) to (14) for the set of temperatures (T_b, T_{Ln}, T_a) measured at each ATS rod are presented as the "nominal" case, whereas the results when the temperature at the base of the rods is averaged between the T_b of ATS rod 1 and ATS rod 2 are presented as the "averaged" case. The latter is considered a solution to reduce the effect of the difference in height between the booms on the ATS temperature profiles; that is, according to the hypothesis introduced in Eq. (14). Namely, we assume that both ATS rods present the same temperature profile under the same wind condition. The unknowns (V_{Boom1}, α) were selected to solve the non-linear equation system, and V_{Boom2} and V_h were obtained from them. Finally, a comparison of the relative error between the horizontal wind speed and angle obtained through the retrieval, V_h and α, and the actual velocity field implemented in the simulation at the entrance of the control volume (i.e., the unperturbed conditions) are included in the last two columns. Similarly, Table 3 presents a comparison of the relative errors for each of the four theories considered for the cross-flow Nusselt modeling, based on which we concluded that the best approach to be implemented in the retrieval is the model proposed by Fand and Keswani (1972) because it resulted in the lowest relative errors in the estimation of both V_h and α compared with the other three theories.

The solution for $V_{Inlet} = 8$ m/s is represented in Fig. 6, where F_1 and F_2 are the solution field of each of the equations for (V_{Boom1}, α) and each Nusselt model that is used. In this figure, the intersection of both solution fields with the plane $F(V_{Boom1}, \alpha) = 0$ provides the solution curve for each equation separately and for each Nusselt model. When the corresponding solution curves of a specific model intersect, the values of (V_{Boom1}, α) at this point represent the solution of the system of equations, which is unique for the specified range of α. The disagreement between the Nusselt models mentioned in Section 3 can

be observed here; that is, those that predict higher Nusselt values for the same Reynolds number produce lower wind speed values for V_{Boom1}. As can be observed, the Whitaker and Perkins approaches for V_{Boom1} exceed the 8 m/s of the horizontal wind speed field, while Fand's $V_{Boom1} < 8$ m/s.

A small deviation from the solution is reported, which should be along the $\alpha = 60°$ axis for all the Nusselt approximations because the incident velocity field was set to this angle in the simulations. This mismatch is associated with the small difference in the temperature profiles along the ATS rods because of the 5-cm difference in height between the booms with respect to the rover deck, introducing a temperature difference along the ATS rods of ~ 0.3 K at T_b and ~ 0.05 K at T_{Ln}. These differences could be higher on Mars, introducing errors in the wind speed and angle calculations provided by this retrieval. In Table 2, the relative error in the nominal wind speed retrieval for $v > 4$ m/s is $\lesssim 10\%$. Then, the average retrieval seems to significantly improve the speed predictions at wind speeds $v \lesssim 6$. For the wind orientations, the average retrieval clearly improved the predictions to $\lesssim 12\%$ for $v \lesssim 10$ m/s. In general, for all cases, the average solution gives the wind speed with an error $< 10\%$ for wind speeds above 4 m/s and the orientation with $\leqslant 12\%$ error for wind speeds below 10 m/s.

3.5.1. Coarse approach

Non-linear equation systems such as that proposed for wind retrieval require an initial point to start the iterative calculation, which must be chosen carefully to avoid spurious solutions or divergence. In addition, this model is highly limited to orientations that can fit within the validity region for α angles. As a result, because of the expected changing conditions on the surface of Mars, a great number of wind speed and direction values are expected to be lost because the 1-Hz temperature profiles cannot be converted in this "refined" model. A more robust approach is considered to increase the wind speed measurement rate to 1 Hz.

We propose a "coarse" approach to first solve the problem only for wind speed, neglecting the effect of the true incidence angle at each ATS rod and the forced convection along the rods ($\beta \sim \alpha$). This means that only normal forced convection to the ATS is considered when shaping the thermal profile along the ATS rods, which simplifies the geometry of the problem. Similar simplifications when modeling the average Nusselt distribution over heated rods have been performed in previous wind sensor concepts on Mars' surface, such as the perpendicular hot films of the Viking 1 wind sensor (Kynkäänniemi et al., 2017). The modulus of the horizontal velocity vector $|\overline{V}_h|$ is computed by applying the area properties of the irregular trapezium that is formed by the two normal components of this velocity vector to the axes of the booms and the constant angle between booms, which is 120°. Fig. 5 emphasizes this approach in red. It is possible to calculate the diagonal of the trapezium; that is, the module of the horizontal wind vector, by calculating sides c and b from values d and a. Assuming $V_{Boom1} \sim d$ and $V_{Boom2} \sim a$, this modulus can be computed as:

$$|\overline{V}_h| = \sqrt{\frac{(a \cdot d + b \cdot c) \cdot (a \cdot c + d \cdot b)}{a \cdot b + d \cdot b}}. \tag{15}$$

This wind speed provides an initial point for solving the non-linear equation system, together with an initial angle α, which can be set, for instance, to 45°. Although the angle is not measured in this approach, this coarse evaluation is notably more robust because it can be applied without any restriction to the set of V_{Boom1} and V_{Boom2} values that are provided. The overestimation from the Whitaker (McAdams, 1954) approach in the CFD studies (see Fig. 6) provided a good solution for estimating wind speed when the wind direction did not fulfill the retrieval requirements, as explained in Section 4.

Table 2

Retrieval results from the model as proposed by Fand and Keswani (1972), which was applied to simulations for a range of characteristic wind speeds [2, 20] m/s and 60° with respect to $+X_{RNAV}$, clockwise. "Nominal" refers to actual temperature values, and "Average" refers to the results when the temperatures at the bases of both ATS rods were averaged. V_{Boom1} and V_{Boom2} are the wind speed values from ATS rod 1 and ATS rod 2; V_h is the modulus of the horizontal wind vector; and α is the angle between the horizontal wind vector and Boom 2, whose theoretical value is 60° according to the input parameters of the simulation. The relative errors for both the horizontal wind speed and direction are also included.

V_{Inlet} [m/s]	Case –	V_{Boom1} [m/s]	V_{Boom2} [m/s]	V_h [m/s]	α [°]	$\left\|\frac{V_{Inlet}-V_h}{V_{Inlet}}\right\| \cdot 100$ [%]	$\left\|\frac{60°-\alpha}{60°}\right\| \cdot 100$ [%]
2	Nominal	0.52	0.47	0.52	31.35	74.0	46.1
	Average	1.21	1.22	1.26	62.01	37.0	3.35
4	Nominal	2.98	2.75	2.99	38.79	25.3	35.4
	Average	3.59	3.56	3.69	57.79	7.8	3.7
6	Nominal	5.35	4.97	5.37	40.82	10.5	31.9
	Average	5.99	5.91	6.15	57.02	2.5	4.9
8	Nominal	7.68	7.19	7.72	42.78	3.5	28.7
	Average	8.27	8.16	8.49	56.77	6.1	5.4
10	Nominal	9.85	9.13	9.9	40.05	1.0	33.3
	Average	10.71	10.40	10.92	52.65	9.2	12.3
16	Nominal	14.66	14.70	15.16	60.80	5.3	1.3
	Average	14.56	15.36	15.51	73.68	3.1	22.8

Table 3

Comparison of the retrieval relative errors in horizontal wind speed and direction; that is, $Err.|_{V_h}[\%] = \left|\frac{V_{Inlet}-V_h}{V_{Inlet}}\right| \cdot 100$ and $Err.|_{\alpha}[\%] = \left|\frac{60°-\alpha}{60°}\right| \cdot 100$, when applying each cross-flow Nusselt number theory to the temperature measurements recovered at simulations over the REMS booms geometry described in Table 2. "*Fand*" refers to the results when using the theory developed by Fand and Keswani (1972), "*Whitaker*" by Van Der Hegge Zijnen (1956), "*Perkins*" by Perkins and Leppert (1964), and "*McAdams*" by McAdams (1954). "Average" refers to the results when temperatures at the base ATS rods were averaged, whereas "Nominal" refers to the results when the actual temperatures collected at each ATS rod were used.

V_{Inlet} [m/s]	Case –	$V_h\|_{Fand}$ Err.[%]	$\alpha\|_{Fand}$ Err.[%]	$V_h\|_{Whitaker}$ Err.[%]	$\alpha\|_{Whitaker}$ Err.[%]	$V_h\|_{Perkins}$ Err.[%]	$\alpha\|_{Perkins}$ Err.[%]	$V_h\|_{McAdams}$ Err.[%]	$\alpha\|_{McAdams}$ Err.[%]
2	Nominal	74.00	46.10	87.50	49.99	68.50	49.98	68.50	49.94
	Average	37.00	3.35	93.00	30.33	69.50	49.97	69.50	49.92
4	Nominal	25.30	35.40	52.00	49.86	52.25	50.00	54.25	50.00
	Average	7.80	3.70	7.25	26.41	24.25	47.53	18.75	45.02
6	Nominal	10.50	31.90	19.67	46.16	44.83	50.00	43.83	50.00
	Average	2.50	4.90	50.00	22.52	4.67	29.94	4.50	31.33
8	Nominal	3.50	28.70	5.63	41.36	7.00	43.38	9.00	45.29
	Average	6.10	5.40	10.63	19.62	10.50	16.80	11.13	22.50
10	Nominal	1.00	33.30	3.10	43.03	1.50	40.04	3.70	43.89
	Average	9.20	12.30	12.90	23.98	11.60	16.93	12.80	29.59
16	Nominal	5.30	1.30	2.13	7.92	6.93	6.03	4.06	2.13
	Average	3.10	22.80	1.44	13.69	5.25	8.69	1.31	19.36

3.6. ATS retrieval process

We propose two levels of processing for wind retrieval calculations as an alternative to the non-operational REMS WS for nighttime wind retrievals or any other future instruments, such as HABIT. Fig. 7 describes this concept.

The temperature readings from both REMS ATS rods are first processed and "cleaned" for use in the calculation of the fluid temperature T_f and the average m-parameter, $\overline{m}$, over each ATS rod estimation. For this step, REMS pressure sensor (PS) values and all temperature readings must be known, the "confidence level" of each boom must be satisfactory according to the standards of each instrument so that the measurements are reliable enough, the uncertainty of the temperature readings must be lower than the differences that are used in the retrieval, and the temperature profile must be within the validity limits of the model.

Next, the retrieval is applied by assuming that only the normal component to each ATS rod modifies the temperature profile. The solution of this system provides a coarse intermediate retrieval, which can provide an approximation of the horizontal wind speed modulus at a rate of 1 Hz by using Whitaker (Van Der Hegge Zijnen, 1956) modeling for forced convection around the ATS rods, independent from the wind direction: $|\overline{V}_h| = f(T_f, \overline{m})$.

In the final step, the refined output is reached. The wind speed provided by the coarse approach is used as an initial point for solving the non-linear system of equations, assuming an initial horizontal incidence angle $\alpha = 45°$. Here, the retrieval is based on the model of Fand and Keswani (1972), which provides both the wind speed and direction at a 1-Hz rate from ATS temperature measurements. This step can be applied as long as the wind direction is within the valid region of the algorithm for α (see Fig. 5), where $\overline{V}_h = f(T_f, \overline{m})$; that is, $V_{Boom2}/V_{Boom1} \in [0.88, 1.13]$. The latter condition was expected to be particularly difficult to fulfill when, according to REMS, the direction of dominant winds within a 5-min slot was close to the edges of the validity region; in these cases, one of the ATS rods might be perturbed by the viscous wake of the MSL mast, blinding the rod (and the m-parameter retrieval) from the free-stream and resulting in a V_{Boom2}/V_{Boom1} value outside the "refined" model accepted ratio. Consequently, even though the WS direction values are theoretically within $\alpha \in [12.95°, 107.05°]$ in these scenarios (and allowing for REMS WS wind direction errors of ±30° for front winds and ±45° for rear winds), the strict "refined" approach conditions might not be fulfilled for some 5-min slots and no numerical solution is possible. In summary, physical obstacles, such as the MSL mast, would affect the retrieval output in both "coarse" and "refined" cases.

4. Results and discussion

The purpose of this work was to provide specific examples that show proof of concept in a field (i.e., on the surface of Mars) of the developed
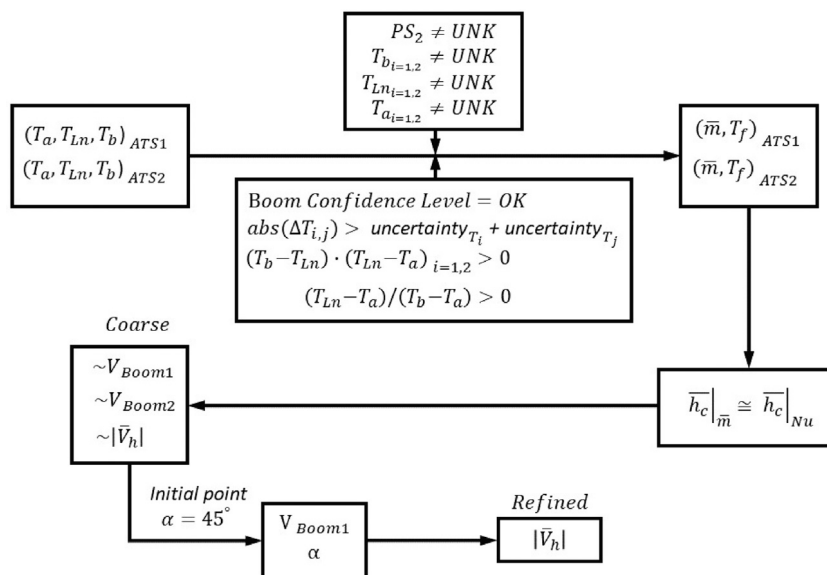
Fig. 7. Proposed algorithm for wind retrieval on the surface of Mars from the REMS ATS temperature readings (see text for details). UNK refers to an "unknown" value in the Planetary Data System (PDS) terminology.

wind retrieval method, not to analyze the entire MSL dataset for every mission sol. Thus, only a subset of results is shown. These results were compared with REMS WS data that are publicly available from the PDS (Gómez-Elvira, 2013a,b,c). As explained in Section 2.1, REMS nominal measurements consist of the first 5 min of every hour at a 1-Hz sampling rate, and the WS provides wind speed values averaged every 5 min. In nominal scenarios, only one point every hour is provided, which is insufficient to properly validate the retrieval performance. Consequently, this analysis focused on mission sols with more extended acquisitions; that is, with more hours where REMS was measuring the entire hour at a 1-Hz rate. Furthermore, to discard possible extra artifacts caused by direct solar radiation, we considered periods where the Sun was already hidden but the temperatures were not yet low enough to arrest acquisition or corrupt the data packages (note that the WS wind retrievals used for comparison suffer from electronic noise at very low temperatures). Thus, this analysis mostly focused on evening hours, from 18:00 to 21:00 Local Mean Solar Time (LMST).

Wind speeds and directions are simultaneously presented to contextualize the rover orientation and wind direction, which affected the validity region of the algorithm and indicated the presence of physical obstacles. It should be noted that the preferred rover orientation for WS wind retrieval; that is, with the rover facing the incoming wind with Boom 2, is not within the valid range for the proposed retrieval. For those sols that were dedicated to wind measurement campaigns, when more extended WS acquisitions were available, the rover heading was prioritized according to the needs of the WS retrievals. For the case of Bagnold Dunes campaign (Newman et al., 2017), some of the sols were suitable for the comparison of the model with REMS WS values; for example, some sols had extended acquisitions in the evening and rover headings that allowed the wind vectors to enter the ATS retrieval model's validity range.

Next, we discuss a set of six sols as examples of situations where (1) the wind speed and direction were not properly retrieved, (2) the wind speed estimation was similar to the WS values when the wind orientation with respect to the rover was not suitable for the refined retrieval, and (3) the incoming horizontal wind vector was (allowing for REMS WS wind direction errors of ±30° for front winds and ±45° for rear winds) within the limits of the refined retrieval method. These sols were selected from the 60 sols of the MSL mission with a higher number of extended acquisitions (a continuous observation of 1 h at 1 Hz) and within the operative time of the WS (sol 0 to 1491), plus sol

730, in which the extended acquisition was within the optimal window of time for the evening (from 18:00 to 21:00 LMST).

The measured wind speeds from the coarse method using the Whitaker approach and averaged over 5 min were retrieved ($V_{5mWhitaker}$). Similarly, both the coarse and refined model outputs using the Fand and Keswani (1972) approach were calculated for 20-s and 5-min averages ($V_{20sFand}$ and V_{5mFand}, respectively) in the case of the former approach, and 5-min averages, $V(V1, \alpha)_{5mFand}$, in the case of the refined approach. Even though REMS WS is not validated for wind retrievals with an acquisition frequency higher than 5-min averages, the ATS wind retrieved 20-s values were included for two main purposes. The first was to qualitatively demonstrate that higher-resolution observations of the fluctuating nature of winds can be achieved with this technique. However, to assess the true validity of these rapidly varying observations, the actual scale of the ATS time-response to fluctuating winds should be studied in detail separately by using a reference probe within adequate facilities, such as a wind tunnel under representative Mars near-surface atmospheric conditions. This will be the focus of future work. The second was to illustrate how quickly the wind pattern can change around REMS, for both the ATS rods and WS; that is, when interpreting these results, it must be considered that even though both the WS and the new ATS retrieval are averaged over the same period, the averages are not performed over the same points in time within that period. This is because corrupted packages for the WS, constrained to the WS dice outputs specified in Section 2.1, do not have to be corrupted for the ATS temperatures (such as electronic noise or any of the exclusion factors considered in the filtering of the dataset when applying the retrieval to the air temperatures, see Fig. 7), and vice versa. Because these 5-min slots for REMS (V_{WS}) did not always include the same points for the calculated wind speed values from the retrieval, it represented a source of mismatch between velocity measurements, whose variability can be observed in the 20-s averages. The wind directions were included using the standard meteorological definition as the direction from which the wind blows. Here, the winds coming from north direction set the reference at 0°, clockwise. The orientation of the forward direction of the rover or X_{RNAV} ("Yaw"), the angle that was measured by the REMS WS ("Angle$_{WS}$"), and the angle that was provided by the refined solution ("Angle$_{Fand}$") were included in 5-min slots. The values shown are, in both cases, the most common values, which is the criterion followed by the WS angle retrieval. Here, the two boundaries that limit the valid range of the refined approach

are highlighted with dashed red lines; that is, valid wind directions that are equivalent to an $\alpha \in [12.95°, 107.05°]$ are contained between these two boundaries. The 5-min approaches may have missed strong velocity fluctuations whose characteristic time was less than 5 min. Depending on the position, the average was determined from these fluctuations, and the final value could differ from the REMS values, whose 1-Hz wind-speed oscillations are not available at the PDS and thus are not considered as validated.

The shadowed regions correspond to situations where the horizontal wind vector was within the refined valid range between Boom 1 and Boom 2 (including error margins). When interpreting the results, it must be noted that the actual wind vector may not have been within the validity region of the refined approach because of the uncertainty of the WS values. The error bars for the REMS values were included, assuming the reported uncertainty of 20% for the wind speed, $\pm 30°$ for frontal winds and $\pm 45°$ for rear winds, although these values have not been confirmed, as discussed in Section 2.1, after the recalibration consequence of the failure of Boom 1 after landing. Wind speed values and orientations from the proposed retrieval process assumed the same uncertainty as REMS, which was the minimum that the retrieval could provide because it is validated against REMS WS dataset.

Fig. 8 corresponds to mission sol 1211 as an example of a retrieval in the evening, immediately after sunset. As can be observed in Fig. 8, in this example, the coarse approach ($V_{20sFand}$, V_{5mFand}, and $V_{5mWhitaker}$) was always available, independent of wind direction. The Whitaker approach (in green) shows relatively good agreement with respect to the REMS measurements. Rear winds caused the artificial constant incidence angle that was measured by REMS (orange) at $\sim 100°$ with respect to North, where no wind speed measurement was possible with only Boom 2 operative and where both ATS rods were partially blinded.

This situation explains why rover operations must be considered for interpreting wind measurements: if the rover is not properly oriented, the wind retrieval output may not be sufficiently representative. Similarly, REMS wind measurements were constrained to front winds; that is, winds coming from the hemisphere in front of the rover (Viúdez-Moreiras et al., 2019a). Because of the limitations of the wind directions that the WS could retrieve, typical secondary flows that were present alongside dominant flows could be captured in the 5-min window. This means that within the REMS WS 1-Hz dataset, secondary winds, or winds from directions that occurred over only a small portion of the 5-min period considered, are also counted when performing the 5-min wind speed averages. In contrast, if the rover is not properly oriented, the dominant wind directions could be mostly missed and the WS output would characterize secondary winds. In general, this orientation was not prioritized for wind measurements, except for a few specific campaigns, such as that described in Newman et al. (2017). Therefore, the uncertainty in wind measurements may have increased with respect to the original estimations of Newman et al. (2017) and Gómez-Elvira et al. (2012). This illustrates why data reported over the entire MSL mission may contain several biases.

The wind speed and direction from the refined approach, $V(V1, \alpha)_{5mFand}$, were reported when the orientation of the rover allowed the wind direction to enter the validity region of the retrieval. Low sensitivity to wind direction changes was noted in the refined output, with a wind direction close to a constant $\alpha \sim 60°$; that is, the refined output did not show any useful determination of wind direction when compared to REMS WS. The coarse retrieval presented, for an assumed WS wind speed error of 20% and with independence of the dominant wind direction, an agreement to the WS speed values $\sim 38\%$ (3 out of 8) of the time between 18:00 and 21:00 LMST.

Fig. 9 presents the results for other sols during the late evening hours from 18:00 to 21:00 LMST. The effect of wind direction variations during evenings, usually clockwise with respect to Z_{RNAV} (Newman et al., 2017), provided better approximations for some sols depending on the orientation of the rover at a specific sol.

For sol 730, the wind speeds were underestimated when the wind direction originated from the front-left quadrant of the rover; that is, wind vectors with $-X_{RNAV}$ and $+Y_{RNAV}$ components. The rover mast blinded the ATS rod from Boom 1, which was in the viscous wake, generating notably lower forced convection. When this direction rolled clockwise and passed the forward direction of the rover; that is, the horizontal wind vectors came from the front-right quadrant with a $-Y_{RNAV}$ component, both ATS rods were properly exposed to airflow and the coarse output described a similar profile to that from the WS. From $\sim 19:45$ onward, WS retrieval disappeared and the coarse output decreased to ~ 0; that is, wind characterization appeared to become too exigent for the WS onboard sensors. Even though the velocities may have been too low for REMS WS to detect, the coarse approach retrieved some values between ~ 0.5 and ~ 2.5 m/s. For the period when the horizontal wind vector was in the front-right quadrant ($-X_{RNAV}$ and $-Y_{RNAV}$ components) and where both ATS and REMS WS data were available, from $\sim 18:30$ onward, the coarse approach and REMS WS wind speed values reached agreement of $\sim 71\%$ (5 out of 7) of the time when both data points were available (to within 20%, the assumed error). According to REMS WS, and allowing for WS wind direction errors of $\pm 30°$, the direction of the dominant wind was near the boundary of the validity region during the evening of this sol. Only one 5-min slot was reported where restrictions were fulfilled in both WS and the refined approach retrievals at some point (and not necessarily coincident); this limitation was expected for these wind orientation scenarios (see Section 3.6).

A similar situation was observed during sol 996 and sol 1096. In the former, a clear roll of the wind direction between 18:00 and 21:00 LMST is visible. Before 19:00, the wind direction was still within REMS WS retrieval's valid range (i.e., the front-left quadrant), with an underestimation of the coarse output. Between $\sim 19:00$ and $\sim 19:25$, the oscillation in direction values was outside the field of view of the WS; that is, winds came from the rear-left quadrant ($+X_{RNAV}$ and $+Y_{RNAV}$ components), and again from $\sim 19:35$ to $\sim 20:35$, with a short 10-min period from $\sim 19:25$ to $\sim 19:35$ when winds entered in the front-left quadrant. From $\sim 20:30$ onward, winds finally entered the front-right quadrant ($-X_{RNAV}$ and $-Y_{RNAV}$ components). Here, the coarse description seemed to be close to REMS WS speeds. In the shadowed region, the coarse approach provided the wind speed, allowing for REMS WS errors of 20% in speed, for $\sim 53\%$ (8 out of 15) of time between 18:30 and 21:00 and for $\sim 88\%$ (7 out of 8) of the time from 19:30 onward when WS points were available.

During sol 1096, most of the evening had winds coming from the front direction, oscillating between the front-left ($-X_{RNAV}$ and $+Y_{RNAV}$ components) and front-right ($-X_{RNAV}$ and $-Y_{RNAV}$ components) quadrants, because of the orientation of the rover, which was suitable for REMS WS but outside the valid retrieval region for the refined output. The coarse approach, however, described the wind speed in agreement to the available REMS WS speed values (to within 20%, the assumed WS error) for $\sim 77\%$ (17 out of 22) of the time between 18:30 and 21:00, demonstrating its robustness toward wind direction oscillations. During sol 1169, where from $\sim 19:15$ to $\sim 20:25$, desired orientations for the refined approach were dominant according to REMS WS values, the agreement between WS speed values and retrieval values, allowing for WS errors of 20%, was $\sim 69\%$ (9 out of 13) of the time in the coarse case according to the available WS data points. In the shadowed region, the refined algorithm recorded wind speed and directions that matched, assuming WS errors of 20% in speed, $\pm 30°$ in front wind orientations, and $\pm 45°$ in rear winds, $\sim 69\%$ (9 out of 13) and $\sim 77\%$ (13 out of 17) of the time, respectively, to REMS WS values (when available).

For sol 1172, the coarse approach provided a worse estimation of the wind speed with respect to sol 1169 the more that the dominant wind orientation approached the rover's front direction, clockwise. This result could be explained by mast wake interference. From 18:00 to 19:00, the dominant wind directions came from the front-left quadrant
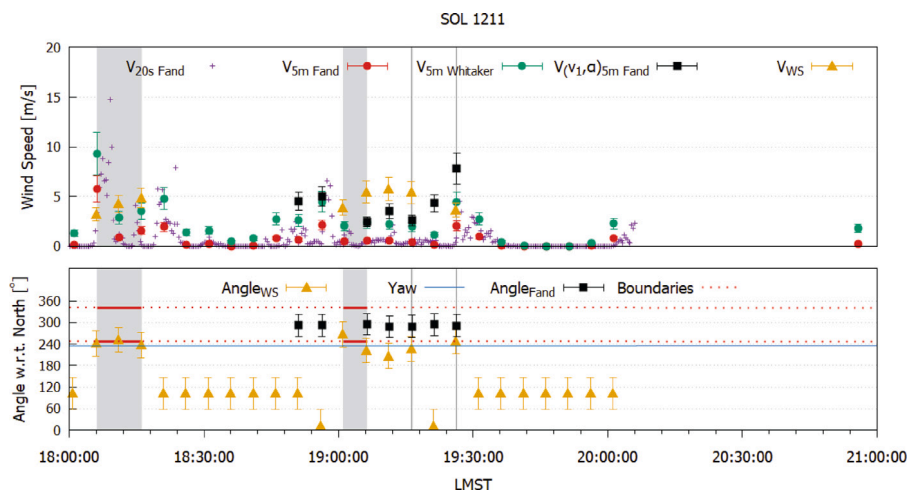
Fig. 8. Results for the evening time from 18:00 to 21:00 LMST on sol 1211 including the wind speed (V_{WS}) and horizontal angles with respect to North ($Angle_{WS}$), clockwise, as provided by REMS WS, and results from the retrieval when applying the proposed Nusselt approximations by both Fand and Keswani (1972) ($V_{20sFand}$ in 20-s averages, V_{5mFand} in 5-min averages) and Van Der Hegge Zijnen (1956) ($V_{5mWhitaker}$ for 5-min average) in the "coarse" approach, and the Fand and Keswani (1972) for the "refined" case [$V(V1, \alpha)_{5mFand}$] in 5-min averages, where $V1$ refers to V_{Boom1}). The rover orientation with respect to North (Yaw) is included. The shadowed regions are periods when the horizontal wind vector (including error margins) retrieved from WS data suggested that the true wind direction was within the boundaries of the "refined" ATS retrieval's validity (the range of direction between the red dotted or dashed lines). However, "refined" retrievals are often missing from the shadowed regions or present outside these regions. This corresponds to times when the ATS (and WS) retrieved wind directions differed, as explained in Section 3.6. The wind directions were included using the standard meteorological definition of the direction from which the wind blows, with the North direction set as the reference at 0°, clockwise. (For interpretation of the references to color in this figure legend, the reader is referred to the web version of this article.)

($-X_{RNAV}$ and $+Y_{RNAV}$ components); that is, outside the valid region of the refined approach. The refined wind speed values matched, allowing for WS errors of 20%, the WS values ~ 60% (6 out of 10) of the time until ~ 19:05, when the refined estimations were available. Similarly, the coarse approach agreed with WS values ~ 66% (8 out of 12) of the time for the same period when the coarse estimations were available, and ~ 36% (8 out of 22) of the time between 18:00 and 21:00 LMST. As can be observed, 19:00 to 20:00 was not an extended-acquisition hour, which supports the need to use extended-acquisition sols to compare the proposed retrieval with REMS measurements. From 20:00 onward, the WS wind direction margins reached the boundaries of the refined approach and moved into this region over time; however, both coarse and refined retrievals underestimated wind speed according to the WS.

Finally, sol 1416 closed the analysis with a different rover orientation. This sol was part of the wind-measurement campaign in Bagnold Dunes (Newman et al., 2017). As can be seen, the orientation of the rover, which was set for REMS WS measurements, was not appropriate for the proposed algorithm with respect to the dominant wind directions because the rover front direction was outside the valid measurement region of the refined approach, partially blinding the ATS rod from Boom 1. However, because of the oscillation of the wind around the rover front direction, the refined solution partially captured the wind speed pattern. Between 18:05 and ~ 18:50, the coarse approach agreed ~ 78% (7 out of 9) of the time with REMS WS wind speeds for the same period (to within 20%, the assumed WS error in wind speeds).

As the current retrieval algorithm only outputs wind directions near $\alpha \sim 60°$, it provides no useful wind direction measurement at present.

5. Conclusions

We proposed a novel method based on available REMS/MSL ATS temperature data from the PDS (Gómez-Elvira, 2013a,b,c) as an alternative technique that may eventually be able to provide the NASA MSL mission with wind information, after the complete failure of the WS reported in sol 1491. We illustrated our methodology with a few evening scenarios of REMS Martian observations, from 18:00 to 21:00 LMST, and for a limited range of horizontal wind directions. This was performed by comparing the results with REMS WS 5-min average data

points. This retrieval could also be applied to the InSight, ExoMars 2022, and NASA 2020 missions because they use similar ATS concepts. This means that a limited but valid wind characterization could be performed on Mars by more than one sensor at different locations on the surface of the planet simultaneously, which could help to characterize near-surface winds for the planet (Viúdez-Moreiras et al., 2019a).

The algorithm was applied to several MSL sols as examples of the different limitations and potentialities of the retrieval method. Assuming a REMS WS error of 20% in wind speeds, we demonstrated agreement between the retrieval wind speed "coarse" estimations and the WS wind speed data points from ~ 36% to ~ 77% of the time between 18:00 and 21:00 LMST. This estimation did not require the wind orientation to be previously known.

Similarly, assuming a REMS WS error of ±30° in front wind orientations (winds approaching the Curiosity rover from ±90° with respect to the front direction or $+X_{RNAV}$) and ±45° in rear winds (winds approaching the rover from +90° to 270° with respect to $+X_{RNAV}$), the retrieval "refined" wind directions were compared to the REMS WS direction values between 18:00 and 21:00 LMST when the dominant wind direction was within the established validity region, $\alpha \in [12.95°, 107.05°]$. Here, α is the horizontal angle clockwise from REMS Boom 2, pointing to the front of the Curiosity rover, relative to Boom 1. However, from the 5-min wind direction comparison, we concluded that this technique is still under development, as it cannot yet determine whether the wind direction is within the range of wind directions for which the method is deemed to be suitable; that is, the direction values were close to a constant $\alpha \sim 60°$, and thus they did not demonstrated yet useful wind direction information. Nevertheless, this is a promising method for wind speed retrieval, provided that the wind direction is within the validity region.

Furthermore, a new optimal orientation for future rover wind retrievals of 60° clockwise from $+X_{RNAV}$ can be inferred from the model, as an alternative to the currently preferred front orientation for REMS WS acquisitions, which would maximize wind characterization if wind campaigns were performed. A dedicated analysis of the retrieval effectiveness over the entire MSL dataset should be performed first, however, to alter the Curiosity rover operations.

The validation presented in this work cannot offer a resolution higher than the reference used; that is, REMS WS 5-min averages. The
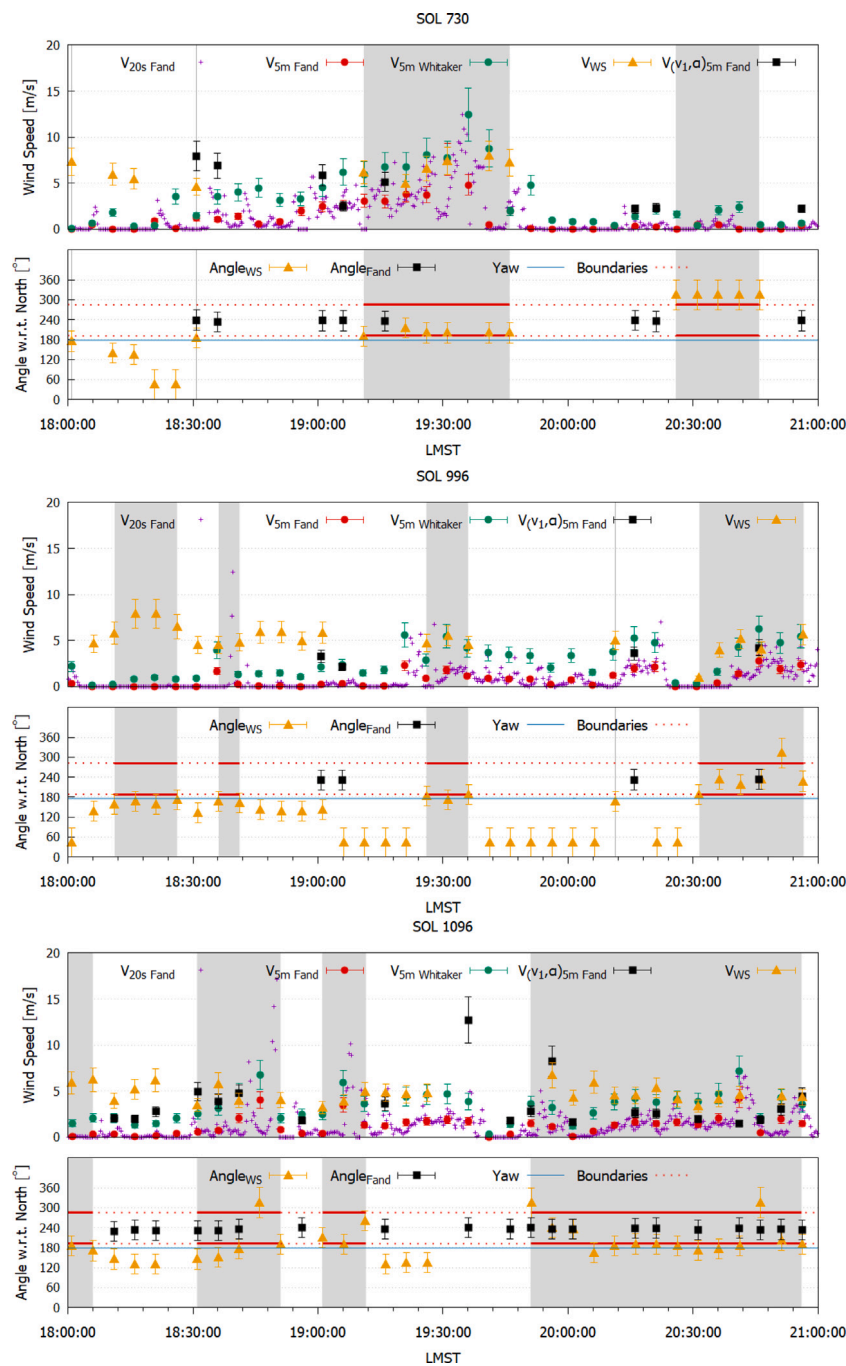
Fig. 9. As in Fig. 8 but for sols 730, 996, 1096, 1169, 1172, and 1416. (For interpretation of the references to color in this figure legend, the reader is referred to the web version of this article.)

validation is also constrained to existing uncertainties of this reference when computing the 5-min points from the 1−Hz WS measurements; retrieval and WS present different definitions for the 1−Hz corrupted packages. The thermal equilibration time of the REMS ATS is reported to be 20 to 80 s (Gómez-Elvira et al., 2014), which may limit the applicability of this method for shorter periods of time. Finally, the method is currently only applicable to evening hours, to avoid direct solar radiation and the usual rapid air temperature changes during the daytime on Mars; it is therefore not yet applicable to most of the diurnal cycle. In this work, we did not explore the application of the retrieval to nighttime conditions beyond 21:00 LMST, when the high electronic noise may affect temperature data availability for the application of the retrieval and WS wind data for comparison.

Further studies will continue this work with the HABIT engineering and qualification model (EQM). Wind tunnel tests of the EQM under Martian near-surface conditions are currently being implemented to demonstrate and calibrate the full operability range of the technique, the actual time response of the retrieval under representative density conditions, and the errors of considering the ATS rectangular-based rods as cylinders when modeling the average Nusselt number in the m-parameter model. Also, new hypotheses are being tested to expand the retrieval acquisition capabilities to diurnal conditions, such as the effect of direct insolation or shadows over the sensors. Future studies will include a broader statistical analysis combining the entire REMS WS dataset, including both daytime and nighttime periods and the results of the HABIT Martian wind tunnel tests to assess the actual capability
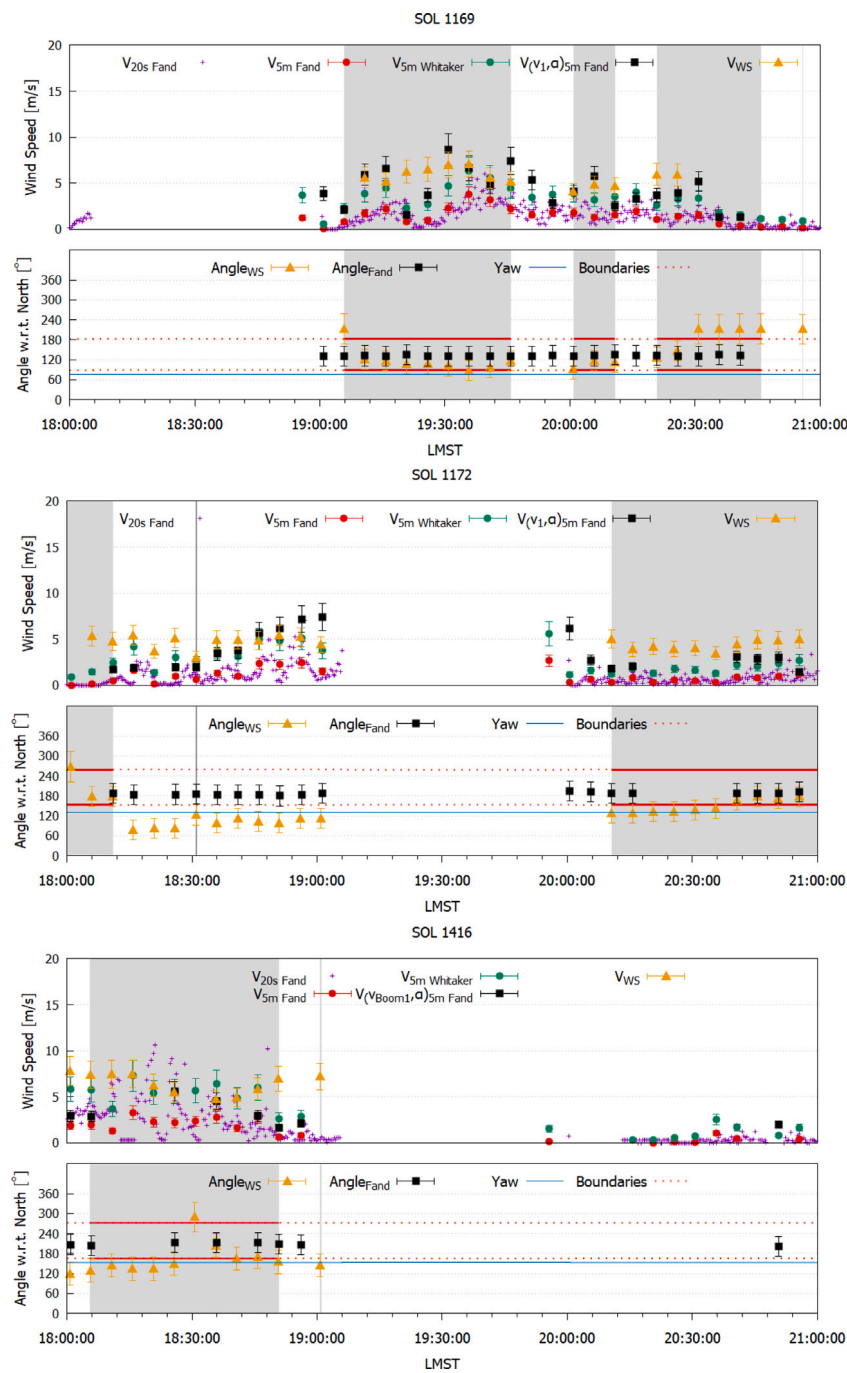
Fig. 9. (*continued*).

of this method for future REMS wind retrievals of horizontal winds on Mars.

References

Achenbach, E., 1971. Influence of surface roughness on the cross-flow around a circular cylinder. J. Fluid. Mech. 46, 321–335.

Basu, S., Richardson, M.I., 2004. Simulation of the Martian dust cycle with the GFDL Mars GCM. J. Geophys. Res. 109 (E11006).

Beese, E., Gersten, K., 1979. Skin friction and heat transfer on a circular cylinder moving in a fluid at rest. Z. Angew. Math. Phys. 30 (1), 117–127.

Berman, D.C., Balme, M.R., Michalski, J.R., Clark, S.C., Joseph, E.C.S., 2018. High-resolution investigations of Transverse Aeolian Ridges on Mars. Icarus 312, 247–266.

Cabeci, T., 1970. Laminar and Turbulent Incompressible Boundary Layers on Slender Bodies of Revolution in Axial Flow. J. Basic. Eng. 92 (3), 545–550.

Cantor, B.A., Kanak, K.M., Edgett, K.S., 2006. Mars Orbiter Camera observations of Martian dust devils and their tracks (September 1997 to January 2006) and evaluation of theoretical vortex models. J. Geophys. Res. 111 (E12002).

Chamberlain, T.E., Cole, H.L., Dutton, R.G., Greene, G.C., Tillman, J.E., 1976. Atmospheric measurements on Mars: the Viking Meteorology Experiment. Bull. Am. Meteorol. Soc. 57 (9), 1094–1105.

Choi, I.G., 1982. The effect of variable properties of air on the boundary layer for a moving continuous cylinder. Int. J. Heat Mass Transfer 25 (5), 597–602.

Curie, N., 1980. Calculation of the Axisymmetric Boundary Layer on a Long Thin Cylinder. Proc. Royal Soc. Lond. A 372, 555–564.

Domínguez, M., Jiménez, V., Ricart, J., Kowalski, L., Torres, J., Navarro, S., Romeral, J., Castañer, L., 2008. A hot film anemometer for the Martian atmosphere. Planet. Space Sci. 56 (8), 1169–1179.

Eswara, A.T., Nath, G., 1992. Unsteady forced convection laminar boundary layer flow over a moving longitudinal cylinder. Acta Mech. 93 (1–4), 13–28.

Fand, R.M., Keswani, K.K., 1972. A continuous correlation equation for heat transfer from cylinders to air in crossflow for reynolds numbers from 10^{-2} to $2x10^5$. Int. J. Heat Mass Transfer 15 (3), 559–572.

Fonseca, R.M., Zorzano, M.-P., J., M.-T., 2018. Planetary boundary layer and circulation dynamics at Gale Crater, Mars. Icarus 302, 537–559.

Glauert, M.B., Lighthill, M.J., 1955. The axisymmetric boundary layer on a long cylinder. Proc. Royal Soc. Lond. A230, 189–203.

Gómez-Elvira, J., 2013a. Mars Science Laboratory Rover Environmental Monitoring Station RDR. NASA Planetary Data System Data V1.0, MSL–M–REMS–6–ADR–V1.0.

Gómez-Elvira, J., 2013b. Mars Science Laboratory Rover Environmental Monitoring Station RDR. NASA Planetary Data System Data V1.0, MSL–M–REMS–4–ENVEDR–V1.0.

Gómez-Elvira, J., 2013c. Mars Science Laboratory Rover Environmental Monitoring Station RDR. NASA Planetary Data System Data V1.0, MSL–M–REMS–5–MODRDR–V1.0.

Gómez-Elvira, J., Armiens, C., Carrasco, I., Genzer, M., Gómez, F., Haberle, R., Hamilton, V.E., et al., 2014. Curiosity's rover environmental monitoring station: Overview of the first 100 sols. J. Geophys. Res. 119, 1680–1688.

Gómez-Elvira, J., Armiens, C., Castañer, L., Domínguez, M., Genzer, M., Gómez, F., Haberle, R., et al., 2012. REMS: The Environmental Sensor Suite for the Mars Science Laboratory Rover. Space Sci. Rev. 170, 583–640.

Greeley, R., Arvidson, R.E., Barlett, P.W., Blaney, D., Cabrol, N.A., Christensen, P., Fergason, R.L., et al., 2006. Gusev crater: Wind-related features and processes observed by the Mars Exploration Rover Spirit. J. Geophys. Res. 111 (E02S09).

Grunt, K., Zuraw, A., Pietrowicz, S., 2016. Analysis of Nusselt number distribution in case of a strongly heated, horizontal rod. Therm. Sci. 25, 542–548.

Haberle, R.M., Leovy, C.B., Pollack, J.B., 1982. Some effects of global dust storms on the atmospheric circulation of Mars. Icarus 50 (2–3), 322–367.

Hassler, D.M., Zeitlin, C., Wimmer-Schweingruber, R.F., Ehresmann, B., Rafkin, S.R.C., Eigenbrode, J.L., Brinza, D.E., et al., 2014. Mars' Surface Radiation Environment Measured with the Mars Science Laboratory's Curiosity Rover. Science 343 (6169,1244797).

Hess, S.L., Henry, R.M., Leovy, C.B., Ryan, J.A., Tillman, J.E., 1977. Meteorological results from the surface of Mars: Viking 1 and 2. J. Geophys. Res. 82 (28).

Holstein-Rathlou, C., Gunnlaugsson, H.P., Merrison, J.P., Bean, K.M., Cantor, B.A., Davis, J.A., Davy, R., et al., 2010. Winds at the Phoenix landing site. J. Geophys. Res. 115 (E00E18).

Ismail, A.F., Khulbe, K.C., Matsuura, T., 2015. Gas Separation Membranes: Polymeric and Inorganic. Springer, Includes indexes.

Jaffe, N.A., Okamura, T.T., 1968. The transverse curvature effect of the incompressible boundary layer for longitudinal flow over a cylinder. Z. Angew. Math. Phys. 19 (4), 564–574.

Jones, K.L., Arvidson, R.E., Guinness, E.A., Bragg, S.L., Wall, S.D., Carlston, C.E., Pidek, D.G., 1979. One Mars Year: Viking Lander Imaging Observations. Science 204 (4395), 799–806.

Kahre, M.A., Murphy, J.R., Haberle, R.M., 2006. Modeling the Martian dust cycle and surface dust reservoirs with the NASA Ames general circulation model. J. Geophys. Res. 111 (E06008).

Kalendar, A., Oosthuizen, P.H., 2013. A numerical and experimental study of natural convective heat transfer from an inclined isothermal square cylinder with an exposed top surface. Heat Mass Transf. 49 (5), 601–616.

Karnis, J., Pechoc, V., 1978. The thermal laminar boundary layer on a continuous cylinder. Int. J. Heat Mass Transfer 21 (1), 43–47.

Kee, R.J., Rupley, F.M., Miller, J.A., Coltrin, M.E., Grcar, J.F., Meeks, E., Moffat, H.K., et al., 2000. CHEMKIN Collection, Release 3.6 Reaction Design, Inc., Includes indexes.

Kelly, H.R., 1954. A Note on the Laminar Boundary Layer on a Circular Cylinder in Axial Incompressible Flow. AIAA J. 21 (9), 634.

Kim, W.S., Diaz-Calderon, A., Peters, S.F., Carsten, J.L., Leger, C., 2014. Onboard Centralized Frame Tree Database for Intelligent Space Operations of the Mars Science Laboratory Rover. IEEE Trans. Cybern. 44 (11), 2109–2121.

Kminek, G., Clark, B.C., Conley, C.A., Jones, M.A., M., P., Race, M.S., Rucker, M.A., et al., 2018. Report of the COSPAR Workshop on Refining Planetary Protection requirements for human missions. In: 2nd COSPAR Workshop on Refining Planetary Protection Requirements for Human Missions. Tech. rep..

Kowalski, L., Muñoz, L., Pumar, M., Serres, V., 2010. Multiphysics Simulation of REMS hot-film Anemometer Under Typical Martian Atmosphere Conditions. In: User Presentations and Proceedings CD - COMSOL Conference : Boston, Paris, Bangalore; Fall 2010 Events.

Kynkäänniemi, T., Kemppinen, O., Harri, A.-M., Schmidt, W., 2017. Wind reconstruction algorithm for Viking Lander 1. Geosci. Instrum. Method. Data Syst. 6, 217–229.

Lin, H.T., Shih, Y.R., 1980. Laminar boundary layer heat transfer along static and moving cylinders. Chin. J. Chem. Eng. 3 (1), 73–79.

Madeleine, J.-B., Forget, F., Millour, E., Montabone, L., Wolff, M.J., 2011. Revisiting the radiative impact of dust on Mars using the LMD Global Climate Model. J. Geophys. Res. 116 (E11010).

Makinwa, K.A.A., Huijsing, J.H., 2001. A wind-sensor interface using thermal sigma delta modulation techniques. Sensors Actuators A 92 (1–3), 280–285.

Makinwa, K.A.A., Huijsing, J.H., 2002. A smart wind sensor using thermal sigma-delta modulation techniques. Sensors Actuators A 97–98, 15–20.

Martínez, G.M., Newman, C.N., De Vicente-Retortillo, A., Fischer, E., Renno, N.O., Richardson, M.I., Fairén, A.G., et al., 2017a. The Modern Near-Surface Martian Climate: A Review of In-situ Meteorological Data from Viking to Curiosity. Space Sci. Rev. 212 (1–2), 295–338.

Martínez, G.M., Newman, C.N., De Vicente-Retortillo, A., et al., 2017b. The Modern Near-Surface Martian Climate: A Review of In-situ Meteorological Data from Viking to Curiosity. Space Sci. Rev. 212 (1–2), 295–338.

McAdams, W.H., 1954. Heat Transmission, 3d ed. New York : McGraw-Hill, Includes indexes.

Mueller, D., Abu-Mulaweh, H., 2006. Prediction of the temperature in a fin cooled by natural convection and radiation. Appl. Therm. Eng. 26, 1662–1668.

Murphy, J.R., Leovy, C.B., Tillman, J.E., 1990. Observations of Martian surface winds at the Viking Lander 1 Site. J. Geophys. Res. 95 (B9), 14555–14576.

Murri, D.G., 2010. Simulation Framework for Rapid Entry, Descent, and Landing (EDL) Analysis. In: NASA Engineering and Safety Center Technical Assessment Report 1 (NASA/TM-2010-216867).

Na, T.-Y., Pop, I., 1996. Flow and heat transfer over a longitudinal circular cylinder moving in parallel or reversely to a free stream. Acta Mech. 118 (1–4), 185–195.

Newman, C.E., Gómez-Elvira, J., Marin, M., Navarro, S., Torres, J., Richardson, M.I., Battalio, J.M., et al., 2017. Winds measured by the Rover Environmental Monitoring Station (REMS) during the Mars Science Laboratory (MSL) rover's Bagnold Dunes Campaign and comparison with numerical modeling using MarsWRF. Icarus 291, 203–231.

Newman, C.E., Lewis, S.R., Read, P.L., Forget, F., 2002a. Modeling the Martian dust cycle 1. Representations of dust transport processes. J. Geophys. Res. 107 (E12, 5123).

Newman, C.E., Lewis, S.R., Read, P.L., Forget, F., 2002b. Modeling the Martian dust cycle 2. Multiannual radiatively active dust transport simulations. J. Geophys. Res. 107 (E12, 5124).

Okajima, A., 1982. Strouhal numbers of rectangular cylinders. J. Fluid Mech. 123, 379–398.

Oosthuizen, P., Mansingh, V., 1986. FREE AND FORCED CONVECTION HEAT TRANSFER FROM SHORT INCLINED CIRCULAR CYLINDERS. Chem. Eng. Commun. 42 (4–6), 333–348.

Perkins, H.C., Leppert, J.G., 1964. Local heat-transfer coefficients on a uniformly heated cylinder. Int. J. Heat Mass Transfer 7 (2), 143–158.

Pla-Garcia, J., Rafkin, S.R.C., Kahre, M.A., Gomez-Elvira, J., Hamilton, V.E., Navarro, S., Torres, J., et al., 2016. The meteorology of Gale crater as determined from rover environmental monitoring station observations and numerical modeling. Part I: Comparison of model simulations with observations. Icarus 280, 103–113.

Polkko, J., Harri, A.-M., Siili, T., Angrilli, F., Calcutt, S., Crisp, D., Larsen, S., et al., 2000. The Net Lander atmospheric instrument system (ATMIS): description and performance assessment. Planet. Space Sci. 48 (12–14), 1407–1420.

Race, M., Johnson, J., Spry, J., Siegel, B., C.A., C., 2015. Planetary Protection Knowledge Gaps for Human Extraterrestrial Missions. In: Workshop on Planetary Protection Knowledge Gaps for Human Extraterrestrial Missions Conducted at NASA Ames Research Center March 24-26, 2015 Moffett Field, CA. Tech. rep..

Rafkin, S.C.R., Pla-Garcia, J., Kahre, M.A., Gomez-Elvira, J., Hamilton, V.E., Marín, M., Navarro, S., et al., 2016. The meteorology of Gale Crater as determined from Rover Environmental Monitoring Station observations and numerical modeling. Part II: Interpretation. Icarus 280, 114–138.

Rotte, J.W., Beek, W.J., 1969. Some models for the calculation of heat transfer coefficients to a moving continuous cylinder. Chem. Eng. Sci. 24 (4), 705–716.

Sakiadis, B.C., 1961. Boundary layer behavior on continuous solid surfaces: III. The boundary layer on a continuous cylindrical surface. AIChE J. 7 (2), 467–472.

Sanitjai, S., Goldstein, R.J., 2004. Forced convection heat transfer from a circular cylinder in crossflow to air and liquids. Int. J. Heat Mass Transfer 47 (22), 4795–4805.

Sarvar, F., Poole, N.J., Witting, P.A., 1990. PCB glass-fibre laminates: Thermal conductivity measurements and their effect on simulation. J. Electron. Mater. 19 (12), 1345–1350.

Sawchuck, S.P., Zamir, M., 1992. Boundary layer on a circular cylinder in axial flow. Int. J. Heat Fluid Flow 13 (2), 184–188.

Schoenenberger, M., Cheatwoodt, F.M., Desai, P.N., 2005. Static Aerodynamics of the Mars Exploration Rover Entry Capsule. In: 43rd AIAA Aerospace Sciences Meeting and Exhibit, (0056).

Schofield, J.T., Barnes, J.R., Crisp, D., Haberle, R.M., Larsen, S., Magalhães, J.A., Murphy, J.R., et al., 1997. The Mars Pathfinder Atmospheric Structure Investigation/Meteorology (ASI/MET) Experiment. Science 278 (5344), 1752–1758.

Seban, R.A., 1951. Skin Friction and Heat Transfer Characteristics of a Laminar Boundary Layer on a Circular Cylinder in Axial Incompressible Flow. AIAA J. 18 (10), 671–675.

Seiff, A., Kirk, D.B., 1977. Structure of the Atmosphere of Mars in Summer at Mid-Latitudes. J. Geophys. Res. 82 (28), 4364–4378.

Stewartson, K., 1955. THE ASYMPTOTIC BOUNDARY LAYER ON A CIRCULAR CYLINDER IN AXIAL INCOMPRESSIBLE FLOW. Quaterly Appl. Math. 13 (2), 113–122.

Sullivan, R., Greeley, R., Kraft, M., Wilson, G., Golombek, M., Herkenhoff, K., Murphy, J., et al., 2000. Results of the Imager for Mars Pathfinder windsock experiment. J. Geophys. Res. 105 (E10), 24547–24562.

Tamppari, L., Rodriguez-Manfredi, J.A., de la Torre-Juárez, M., Bridges, N., Conrad, P.G., Genzer, M., Gomez, F., et al., 2015. The Mars Environmental Dynamics Analyzer (MEDA): A Suite of Environmental Sensors for the Mars 2020 Rover. In: AGU Fall Meeting Abstracts. pp. P11B–2097.

Towner, M.C., Patel, M.R., Ringrose, T.J., Zarnecki, J.C., Pullan, D., Sims, M.R., Haapanala, S., et al., 2004. The Beagle 2 environmental sensors: science goals and instrument description. Planet. Space Sci. 52 (13), 1141–1156.

Van Der Hegge Zijnen, B.G., 1956. Modified correlation formulae for the heat transfers by natural and by forced convection from horizontal cylinders. Appl. Sci. Res. 6 (2–3), 129–140.

Velasco, T., Rodríguez-Manfredi, J.A., 2015. Multiphysics Simulation of REMS hot-film Anemometer Under Typical Martian Atmosphere Conditions. In: EGU General Assembly Conference Abstracts, vol. 17. p. 2571.

Vicente-Retortillo, A., Valero, F., Vázquez, L., Martínez, G.M., 2015. A model to calculate solar radiation fluxes on the Martian surface. J. Space Weather Space Clim. 5 (A33).

Viúdez-Moreiras, D., Gómez-Elvira, J., Newman, C.E., Navarro, S., Marin, M., Torres, J., de la Torre-Juárez, M., the MSL team, 2019a. Gale Surface Wind Characterization based on the Mars Science Laboratory REMS Dataset. Part I: Wind Retrieval and Gale's Wind Speeds and Directions. Icarus 319, 909–925.

Viúdez-Moreiras, D., Gómez-Elvira, J., Newman, C.E., Navarro, S., Marin, M., Torres, J., de la Torre-Juárez, M., the MSL team, 2019b. Gale surface wind characterization based on the Mars Science Laboratory REMS dataset. Part II: Wind probability distributions. Icarus 319, 645–656.

White, F., 2011. Viscous Fluid Flow. Mcgraw Hill.

Wilson, C., 2003. The Measurement of Wind on the Surface of Mars (Ph.D. thesis). Linacre College, Oxford University.

Wilson, S.A., Zimbelman, J.R., 2004. Latitude-dependent nature and physical characteristics of transverse aeolian ridges on Mars. J. Geophys. Res. 109 (E10003).

Zurek, R.W., 1982. Martian great dust storms: An update. Icarus 50 (2–3), 288–310.